Cell Reports

Article

An adaptive organelle triad houses lipid droplets for dynamic regulation

Graphical abstract

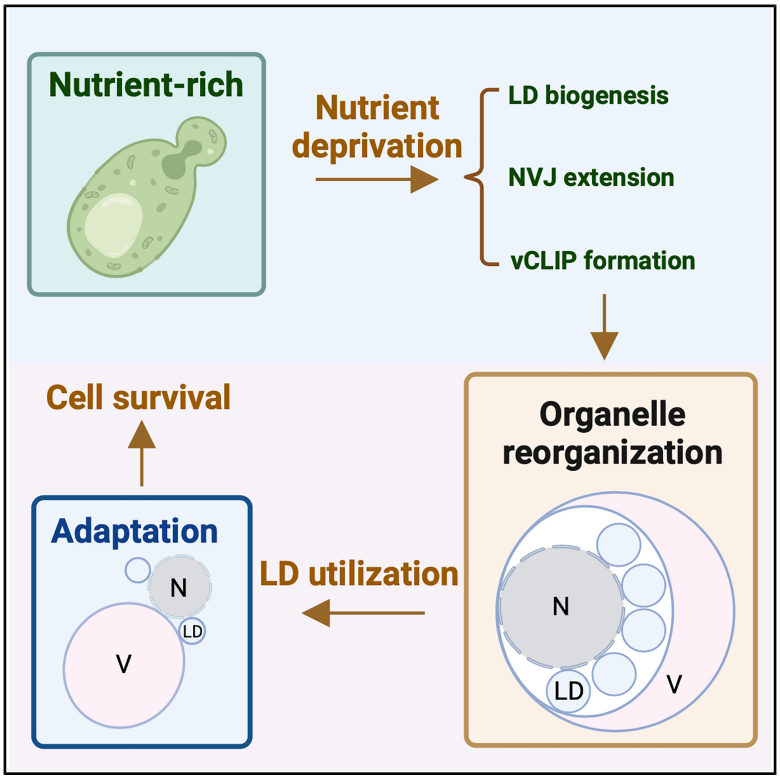

Highlights

- Lactate induces severe metabolic stress and vacuole deformation during nutrient deprivation
- Organelle triad: LDs encircling a nucleus, all enclosed in an enlarged vacuole
- Membrane tethers (NVJ and vCLIP) facilitate organelle triad formation
- This structure promotes efficient LD utilization and cellular adaptation

Authors

Hong Qiu, Can Miao, Cunqi Ye

Correspondence

yecunqi@zju.edu.cn

In brief

Qiu et al. find a novel organelle triad in stressed yeast, comprising an expanded vacuole encapsulating the nucleus encircled by LDs. Membrane-tethered vCLIP and NVJ complexes coordinate this subcellular organization, driving LD turnover to promote cellular survival under stressful conditions.

Qiu et al., 2025, Cell Reports *44*, 115813
June 24, 2025
https://doi.org/10.1016/j.celrep.2025.115813

CellPress

Cell Reports

CellPress
OPEN ACCESS

Article

An adaptive organelle triad houses lipid droplets for dynamic regulation

Hong Qiu,[1,4] Can Miao,[1,4] and Cunqi Ye[1,2,3,5,*]
[1]Zhejiang Provincial Key Laboratory of Cancer Molecular Cell Biology, Life Sciences Institute, Zhejiang University, Hangzhou, China
[2]Department of Reproductive Endocrinology, Women's Hospital, Zhejiang University School of Medicine, Zhejiang, Hangzhou, China
[3]Hainan Institute, Zhejiang University, Sanya, China
[4]These authors contributed equally
[5]Lead contact
*Correspondence: yecunqi@zju.edu.cn
https://doi.org/10.1016/j.celrep.2025.115813

SUMMARY

Cell organelles compartmentalize metabolic reactions and require inter-organelle communications to coordinate metabolic activities in fluctuating nutrient environments. While membrane contacts enable this communication by facilitating metabolite exchange, the functional organization of organelles through these contacts remains underexplored. Here, we show that excess lactate induces severe metabolic stress under nutrient deprivation in the budding yeast *Saccharomyces cerevisiae*, necessitating a rapid life cycle of lipid droplets (LDs) for cellular adaptation. This process uncovers a previously uncharacterized subcellular architecture—an organelle triad—comprising the vacuole, LDs, and the nuclear endoplasmic reticulum (ER). The vacuole undergoes expansion and deformation, enveloping the entire nucleus that is encircled by an orbit of LDs. Formation of this organelle triad depends on the timely and abundant expression of membrane-tethering proteins that mediate vacuole-LD contact sites and nuclear ER-vacuole junctions. This dynamic and reversible subcellular organization ensures efficient LD metabolism to support cell survival under nutrient stress.

INTRODUCTION

To thrive in fluctuating nutrient environments, cells must sense nutrient availability, rapidly activate signaling cascades to transform metabolism, and ultimately sustain cellular homeostasis.[1,2] Nutrient fluctuations generate metabolic signals that orchestrate regulatory processes at both the transcriptional and post-translational levels, enabling cells to adjust biological activities such as energy metabolism and nutrition use for adaptation.[3–5] These adaptive processes also involve the dynamic coordination of cellular organelles, such as autophagic turnover of mitochondria,[6] biogenesis of lipid droplets (LDs),[7,8] and positioning of lysosomes,[9,10] which often depend on inter-organelle communications. In eukaryotes, membrane-bound organelles compartmentalize metabolic reactions, establishing unique chemical environments for efficient and precise control of biochemical pathways.[11] This spatial segregation necessitates inter-organelle communication, often facilitated by membrane contact sites, where metabolic signals conveying nutrient status are relayed and propagated.[12–16] Despite advances in understanding these processes, how closely apposed organelles interpret and respond to changes in nutrition states remains unclear.

Nutrient quality and availability, such as the type of carbon source, are closely tied to specific organelles and their inter-organelle communication to ensure efficient energy production and biomass synthesis. Lactate, as an alternative carbon source and glycolytic metabolite, exhibits distinct metabolic features compared with glucose and plays crucial roles in various physiological and pathological processes.[17,18] For instance, lactate metabolism supports tumor growth[19] and modulates immune responses,[20] highlighting unique cellular strategies to navigate the metabolic networks shaped by lactate. In budding yeast, nutrient deprivation achieved by transitioning cells from a lactate-rich medium to a lactate-minimal medium has uncovered critical adaptive mechanisms. These include PP2A-mediated regulation of autophagy[21–23] and the metabolite *S*-adenosylmethionine-mediated interplay between membrane phospholipid metabolism and histone modification.[24–27] These observations raise important questions about how lipid metabolism and membrane-associated events are leveraged as adaptive strategies during nutrient fluctuations, and how the quality of nutrients impacts these mechanisms.

In this study, we observed a burst in LD production in yeast cells growing in lactate-rich medium when challenged by nutrient deprivation. Under these conditions, respiring cells with excess lactate exhibit the formation of an orbit of LDs, originating from and attached to the outer nuclear membrane (ONM). Concurrently, the vacuole(s) undergo fusion, expansion, and deformation, enveloping the LD-associated nucleus and forming a structurally integrated organelle triad. This undefined subcellular architecture, induced by nutrient stress, is driven by LD biogenesis and requires the vacuole receptor protein Vac8. Vac8

facilitates heterogeneous membrane tethering by competitively interacting with LDO proteins in LDs and Nvj1 in the nuclear endoplasmic reticulum (ER), with their protein expression levels proportionally upregulated under these conditions. Yeast cells confect this organelle triad to enhance LD turnover efficiency, supporting survival during nutrient deprivation. This drastic reorganization of organelles through membrane contact sites demonstrates a functional intracellular continuity in eukaryotes that aids in coping with metabolic stress.

RESULTS

Visual examination of organelle morphology under nutrient stress conditions reveals a vacuolar membrane deformation phenomenon specific to lactate use

Cell organelles respond to changes in nutrient status, such as fluctuations in nutrient quality and availability, facilitating adaptive cellular transitions.[28–30] To explore the functional response of organelles to excessive carbon sources under nutrient deprivation, we subjected prototrophic budding yeast cells, growing logarithmically in different carbon sources, to nutrient deprivation while maintaining the availability of specific carbon sources (Figure 1A). We first compared the growth response of yeast cells undergoing nutrient deprivation in the presence of difference carbon sources, such as glucose, ethanol, glycerol, and lactate. Cells continued to grow after switching to glucose minimal medium, reaching saturation quickly within 8 h (Figure 1B). In contrast, cells in ethanol minimal medium showed a moderately slower growth rate but sustained growth for up to 48 h (Figure 1B). However, under nutrient deprivation conditions with glycerol or lactate, cells experienced growth arrest around 10 h after the switch, with cell numbers barely doubling (Figure 1B). Despite similar growth rates in nutrient-replete conditions with ethanol, glycerol, and lactate (Figure S1A), the differential growth responses to nutrient deprivation suggest that cells growing in glycerol or lactate encounter more metabolic stress. Notably, nutrient stress was more pronounced with lactate use, as substantial cell viability loss occurred after 48 h of nutrient deprivation in lactate minimal medium (Figure 1C), consistent with previous findings.[31]

We then investigated how major organelles, including the ER, mitochondria, vacuoles, peroxisomes, and LDs, respond to these nutrient stress conditions. We visualized these organelles using cells with chromosomally tagged marker proteins fused to GFP at the C terminus. Among all the organelles examined, LDs and vacuoles were the most morphologically responsive to nutrient stress (Figures 1D and 1E and S1B–S1D). LDs increased in number after growth arrest in glucose medium, but this increase was more pronounced and rapid in ethanol and lactate-based minimal medium, occurring immediately upon the switch (Figures 1D and 1F). LDs formed under these conditions showed differences in dynamics and sizes, forming faster with lactate (Figure S1E) and becoming larger with ethanol after 24 h (Figure S1F). In glycerol medium, only a few LDs were observed after nutrient deprivation (Figure 1D).

For vacuoles, we found that the small vacuoles present under nutrient-replete conditions fused into a larger vacuole, gradually increasing in size under nutrient deprivation (Figure 1E). Interestingly, in lactate-using cells undergoing nutrient deprivation, we observed an enlarged, donut-like vacuole with a crescent-shaped lumen (Figure 1E), revealing a previously uncharacterized vacuole deformation phenomenon. Quantitative analysis indicated that approximately 60% of the cells exhibited this vacuole phenotype 12 h after exposure to lactate-based nutrient stress, compared with less than 4% found under glycerol-based conditions (Figures 1G and S1G, refer to methods for this structural quantification). This high occurrence rate was associated with the rapid generation of a larger quantity of LDs, suggesting an interplay between LDs and the vacuole in adapting to this nutrient stress condition.

Electron microscopy reveals an integrated organelle triad comprising LDs, the vacuole, and the nucleus under lactate nutrient deprivation conditions

To better characterize this phenomenon in cells subjected to lactate-based nutrient deprivation, we used transmission electron microscopy (TEM) to analyze subcellular architecture. Over a 12-h nutrient deprivation period, we observed a significant reorganization of organelle networks (Figure 2A), with LDs emerging and increasing in size (Figure 2B). We found that most LDs were positioned outside and adjacent to the nucleus (Figure 2A). After 6 and 12 h of nutrient deprivation, the nucleus, surrounded by LDs, was frequently observed to be enclosed within an enlarged vacuole, shaped like a curved sickle or swim ring (Figure 2A). Quantitative TEM analysis revealed a progressive increase in the occurrence of this subcellular structure over the 12-h nutrient deprivation period, with 45% of cells exhibiting this feature at the 12-h time point (Figure 2C). The occurrence rates observed via TEM were slightly lower than those observed with fluorescence microscopy, possibly due to technical variations. This TEM finding confirmed the crescent-shaped vacuole observed under fluorescence microcopy. The structural integration of the vacuole, LDs, and the nucleus resembled a ball bearing (Figure 2D), hence we termed the "subcellular bearing."

Next, we performed three-dimensional (3D) TEM imaging to analyze the subcellular bearing structure further. A 3D reconstruction by tomographic analysis showed that the vacuole formed a tubular ring encompassing the entire nucleus, with LDs sandwiched between the vacuole membrane and the ONM (Figure 2E). Using focused ion beam scanning electron microscopy (FIB-SEM), we reconstituted the subcellular bearing in a single yeast cell. As shown in Figure 2F and Video S1, the vacuole expanded into a sheet-like wrapper around the nucleus, with a compressed lumen. Many LDs were deposited to bridge the vacuole and nuclear periphery, with some located outside the bearing. An aperture in the 3D structure indicated that the nucleus was not fully enclosed by the expanding vacuole (Figure 2F).

Finally, we used spinning disk confocal microscopy to capture this organelle triad along the *z* axis in cells after 12 h of nutrient deprivation. Using Nup60-NLS-CFP for nuclear labeling, Vph1-mCherry for the vacuole, and BODIPY for LDs, 3D analysis confirmed that the nucleus was surrounded by the vacuole, with LDs bridging the ONM and the vacuole, and a clear aperture (Figures 2G and 2H). This observation aligns with the FIB-SEM

CellPress
OPEN ACCESS

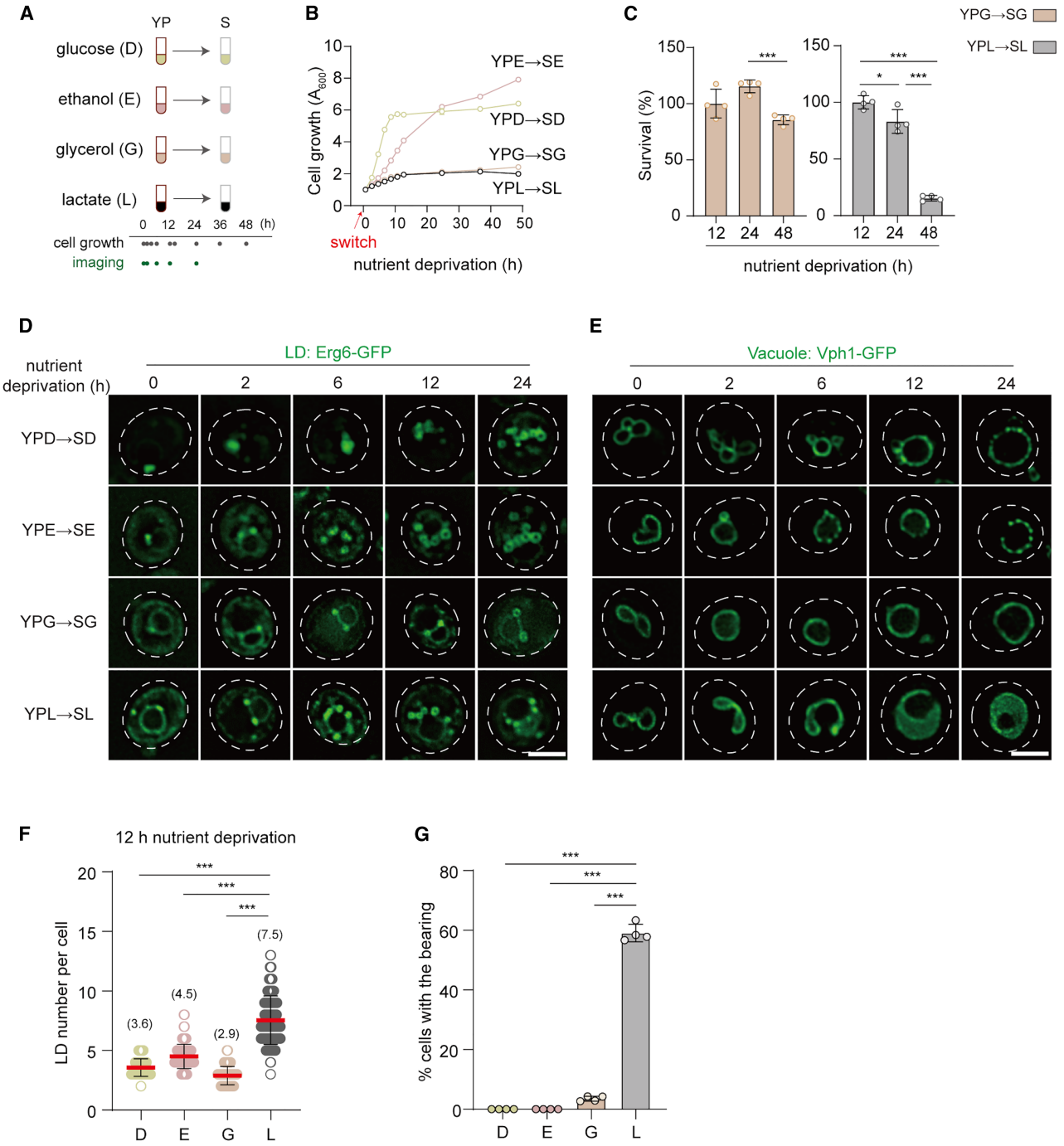

Figure 1. Morphological screening of major organelle responses to nutrient deprivation under varying carbon sources

See also Figure S1.

(A) Schematic of the experimental design.

(B) Growth curves of cells following the indicated medium switch. Data are presented as mean (n = 4 biologically independent samples).

(C) Relative survival rates post-nutrient deprivation. Data are shown as mean ± SD (n = 4 biologically independent samples). *p < 0.05; ***p < 0.001.

(D and E) Live cell imaging showing LDs labeled with Erg6-GFP and vacuoles labeled with Vph1-GFP in WT cells. Scale bar, 2 μm.

(F) Quantification of LD number. Data shown are representative of experiments repeated twice and represented as mean ± SD (n = 200 cells). *** p < 0.001.

(G) Quantification of subcellular bearing formation. Data are represented as mean ± SD (n = 4 independent experiments; >200 cells were quantified per experiment). *** p < 0.001.

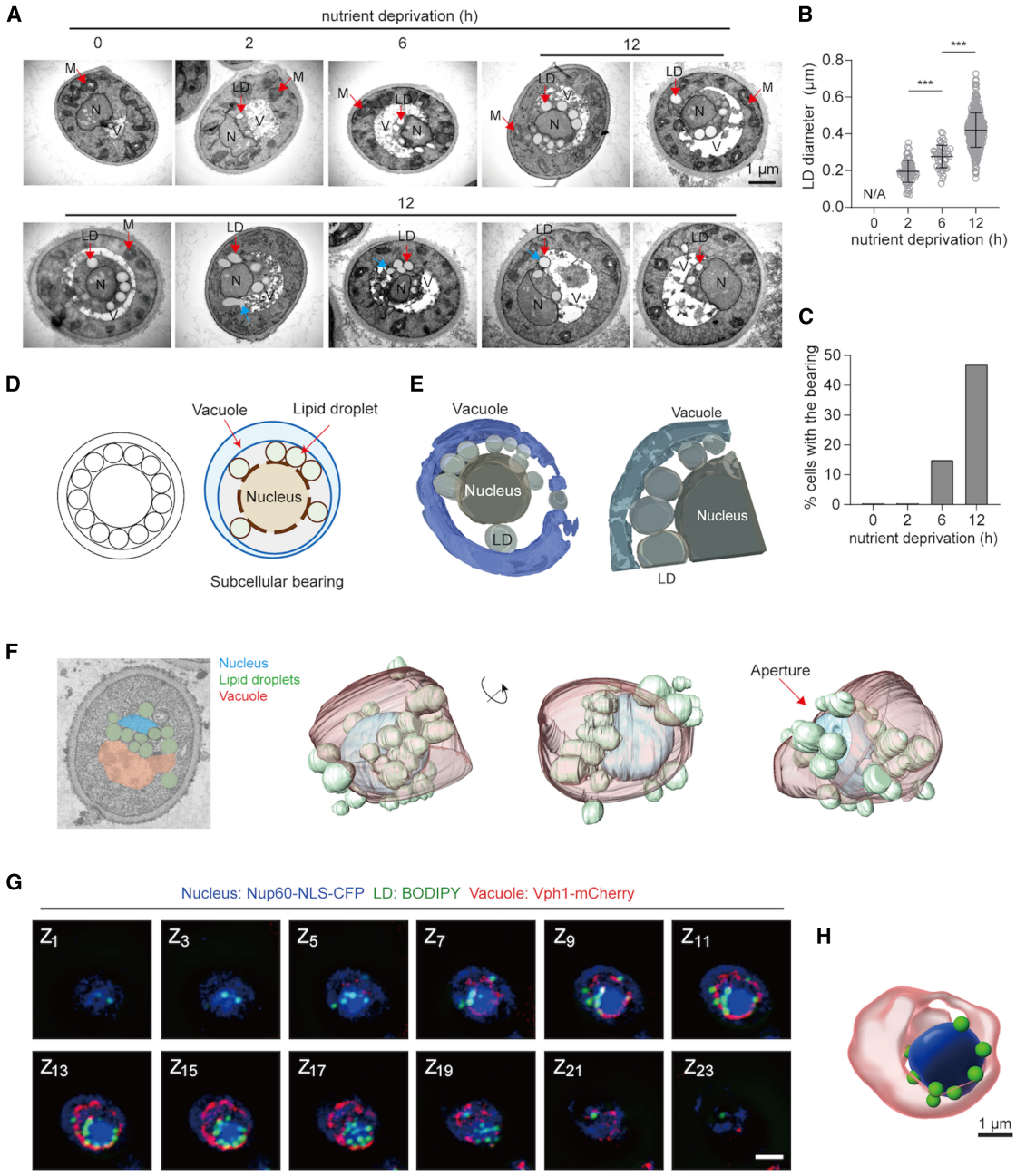

Figure 2. Subcellular organization of the vacuole, LDs and nucleus into a bearing-like structure during nutrient deprivation

See also Video S1.

(A) TEM images. Scale bar, 1 μm. M, mitochondrion; N, nucleus; V, vacuole. Blue arrows indicate LDs likely undergoing lipophagy.

(B) Quantification of LD diameters from TEM images. Data shown are representative of experiments repeated twice and represented as mean ± SD (n = 100, 151, 132, and 415 LDs from TEM images). N/A indicates no LDs observed prior to nutrient deprivation. *** $p < 0.001$.

(C) Percentage of WT cells exhibiting subcellular bearing structures, based on TEM data. We quantified 100 cells for each condition.

(D) Schematic comparison of a mechanical bearing (left) and a subcellular bearing (right).

(E) A 3D reconstruction of the subcellular bearing using electron tomography.

(F) A 3D reconstruction of the subcellular bearing using FIB-SEM.

(G) Confocal spinning-disk microscopy z stack images of a WT cell showing subcellular bearing formation. Nucleus labeled with Nup60-NLS-CFP, LDs stained with BODIPY, and vacuole visualized with Vph1-mCherry. Scale bar, 2 μm.

(H) A 3D reconstruction of the subcellular bearing structure derived from the z stack images in (G). Scale bar, 1 μm.

3D reconstruction, demonstrating that the LD-attached nucleus is wrapped by the deformed vacuole.

Assembling the subcellular bearing is dynamic and reversible

To characterize how the vacuole expands to envelop the nucleus and form subcellular bearings over time, we subjected cells to prolonged nutrient deprivation in lactate minimal medium for up to 60 h. Using fluorescence live cell imaging, we examined starved cells at various time points, with the cell nucleus and vacuole labeled with the nuclear pore complex protein Nic96-GFP and the vacuolar-ATPase component Vph1-mCherry, respectively. A standard subcellular bearing, characterized by an enlarge vacuole enveloping the nucleus, was most frequently observed between 6 and 33 h after the onset of nutrient deprivation (Figure 3A, white arrows). During the 12- to 23-h nutrient deprivation window, approximately 40% of cells exhibited this standard bearing (Figure 3B). Additionally, approximately 20% of cells showed a semi-wrapping of the nucleus by the vacuole, which we termed a partial bearing (Figure 3B). After 60 h of nutrient deprivation, most cells displayed a single, spherical, enlarged vacuole abutting the nucleus (Figures 3A and 3B). The percentage of cells with standard or partial bearings increased 6 h after nutrient deprivation, followed by a decrease in cells containing fragmented vacuoles (Figure 3B). These findings suggest that subcellular bearing formation is a dynamic and reversible assembling process under nutrient deprivation conditions.

To further investigate this process, we tracked individual yeast cells under nutrient deprivation using time-lapse, live-cell fluorescence imaging with a confocal spinning-disk microscope. Our observations confirmed that vacuolar wrapping of the nucleus was a dynamic process, involving cycles of vacuole fusion and fission surrounding the nucleus (Figure 3C and Video S2). The enlarged vacuole repeatedly expanded to embrace the nucleus, a process reminiscent of molding plastic (Figure 3C and Video S2). During the 60-min imaging period, the subcellular bearing assembled twice and disassembled three times, highlighting the dynamic and reversible nature of this subcellular structure.

The formation of subcellular bearings requires LD biogenesis

During the process of this lactate-based nutrient deprivation, the number of LDs exhibited dynamic fluctuations over time (Figure 4A). The temporal fluctuations in LD numbers seemed to coincide with the formation of subcellular bearings (Figure 4A), suggesting that LDs may be required for the vacuolar wrapping of the nucleus. To test this hypothesis, we first disrupted LD biogenesis by genetically inhibiting the synthesis of neutral lipids. When the two diacylglycerol acyltransferases responsible for triacylglycerol (TAG) synthesis were abrogated (*dga1Δlro1Δ*), the resulting TAG depletion blocked LD biogenesis under this nutrient deprivation condition (Figures 4B and S2A and S2B). Consequently, the subcellular bearing structure was scarcely observed in these cells (Figures 4B and 4C). However, disrupting sterol esterification by deleting *ARE1* and *ARE2* (*are1-Δare2Δ*) had no significant impact on TAG levels or subcellular bearing formation, although it led to a slight reduction in LD numbers (Figures 4B, 4C, and S2A–S2C). Deletion of *SEI1*, which encodes a crucial protein involved in LD assembly, also disrupted subcellular bearing formation (Figure S2E), with abnormal LD clustering under nutrient deprivation (Figure S2F). These findings indicate that the LDs involved in subcellular bearing formation are TAG rich and crucial for its assembly.

Next, we titrated the availability of the carbon source lactate under nutrient deprivation to disrupt LD biogenesis. After 12 h of nutrient deprivation, TAG levels decreased significantly to approximately 8% and 25% with 0% and 0.02% lactate, respectively, while 0.2% and 2% lactate supported similar levels of TAG production (Figure 4D). Similarly, sterol ester content was significantly reduced with 0% and 0.02% lactate, although to a lesser extent than TAG (Figure S2D). Correspondingly, LDs were sparse in minimal medium containing 0% or 0.02% lactate, while 0.2% lactate led to a moderate reduction in LD numbers compared with 2% lactate (Figures 4E and 4F). These findings indicate that lactate serves as a key carbon source for TAG synthesis and LD formation under nutrient stress. Consistent with the reduction in LD numbers, subcellular bearings were scarcely observed in minimal medium with 0% or 0.02% lactate and were decreased with 0.2% lactate (Figures 4G and 4H). These associative reductions in subcellular bearing formation indicate that TAG-rich LDs play a crucial role in subcellular bearing formation.

While LD biogenesis can serve as a response to alleviate lipotoxic stress,[32–34] we found that blocking TAG production in *dga1Δlro1Δ* cells substantially decreased survivability compared with wild-type (WT) cells (Figure 4I). In contrast, blocking sterol esterification did not impact cell survivability (Figure 4I). This suggests that lactate-fueled TAG deposition for LD biogenesis may serve as a protective mechanism to mitigate lipotoxic stress. Supporting this hypothesis, we observed that reducing the lactate concentration in nutrient deprivation medium resulted in varying degrees of protection against viability loss under nutrient deprivation conditions (Figure 4J). These findings underscore the role of LD biogenesis in mediating the reorganization of subcellular architecture, enabling cells to adapt to nutrient stress.

LDs promote NVJ extension during subcellular bearing formation

The subcellular bearing structure frequently exhibits extensive membrane contacts between the nuclear ER and the vacuole (Figures 2A and 3A), forming a contact site known as the nucleus-vacuole junction (NVJ) (Figure 5A). Given that the NVJ is a site of LD biogenesis,[35–37] we investigated whether LDs promote NVJ extension, thereby facilitating the nuclear ER-vacuole contact for subcellular bearing formation. Consistent with previous findings,[35] LDs produced under this nutrient deprivation condition were tethered around the NVJ (Figure 5B). We quantified the NVJ length using Nvj1-GFP, an NVJ protein residing in the ONM. As expected, the NVJ co-localized with the vacuole marker Vph1-mCherry (Figure 5C). Interestingly, the NVJ extended along the inner ring of the vacuole membrane within the subcellular bearing structure (Figure 5C), concurrently occurring with the vacuole deformation for subcellular bearing formation. The NVJ length exhibited a gradual increase over the 12-h

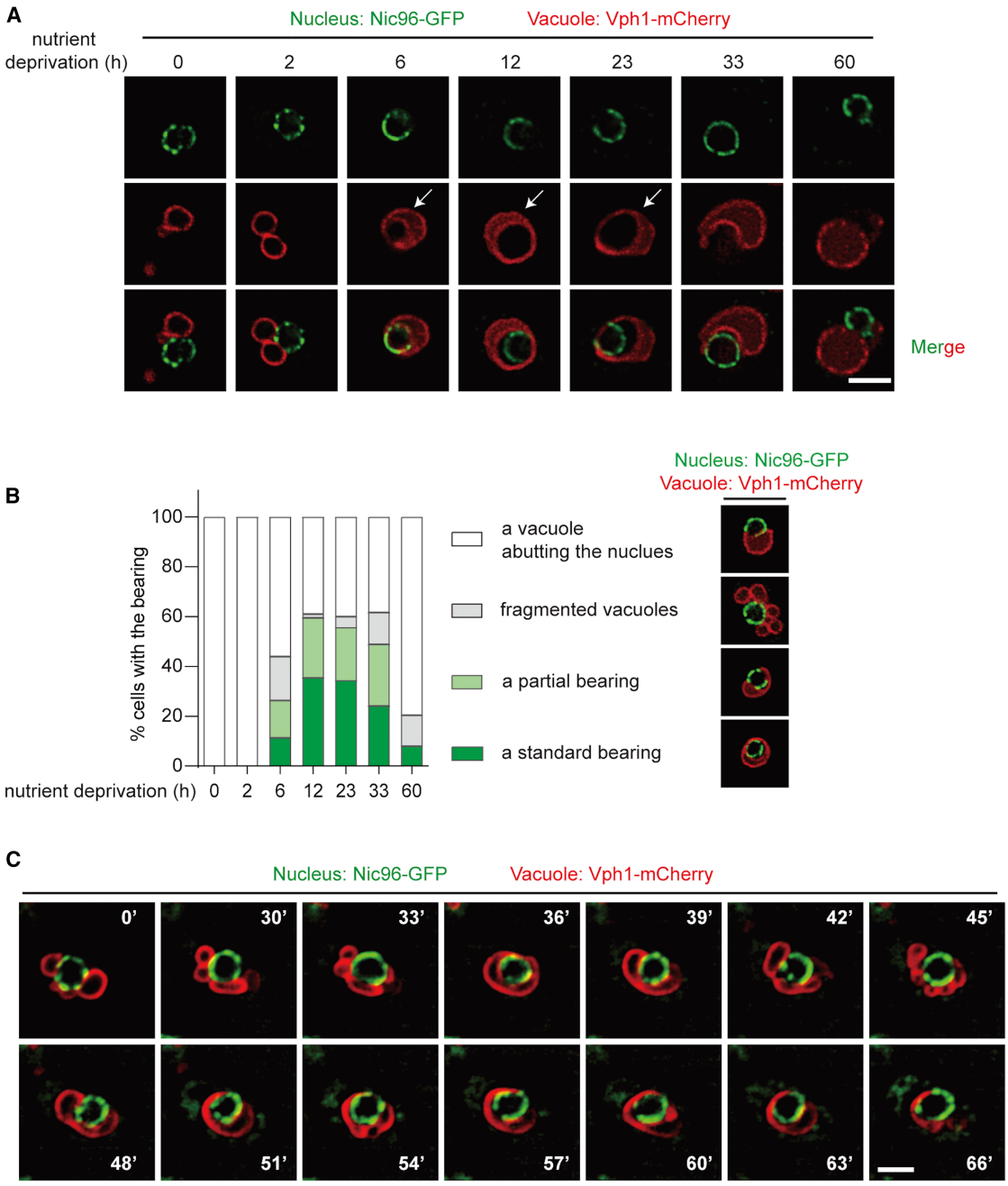

Figure 3. Dynamics and reversibility of subcellular bearing assembly

See also Video S2.

(A) Fluorescence imaging of WT cells showing the nucleus labeled with Nic96-GFP and the vacuole labeled with Vph1-mCherry. Images were taken at indicated times. Scale bar, 2 μm.

(B) Quantification of vacuole morphologies. Data are represented as mean (n = 3 independent experiments; >100 cells were quantified).

(C) Time-lapse imaging of subcellular bearing formation in WT cells with Nic96-GFP and Vph1-mCherry. Images were acquired with a confocal spinning-disk microscope. Scale bar, 2 μm.

nutrient deprivation period (Figure 5D), correlating with the number of LDs generated (Figure 4A).

To visualize the dynamics of nuclear-ER-vacuole contact and LDs during subcellular bearing formation, we performed time-lapse spinning disk microscopy in two strains using three-fluorophores to track combinations of markers (Nvj1-GFP for NVJ, Vph1-mCherry for the vacuole, and AUTODOT for LDs) and (Nvj1-GFP for NVJ, Sec63-mCherry for the ER, and AUTODOT

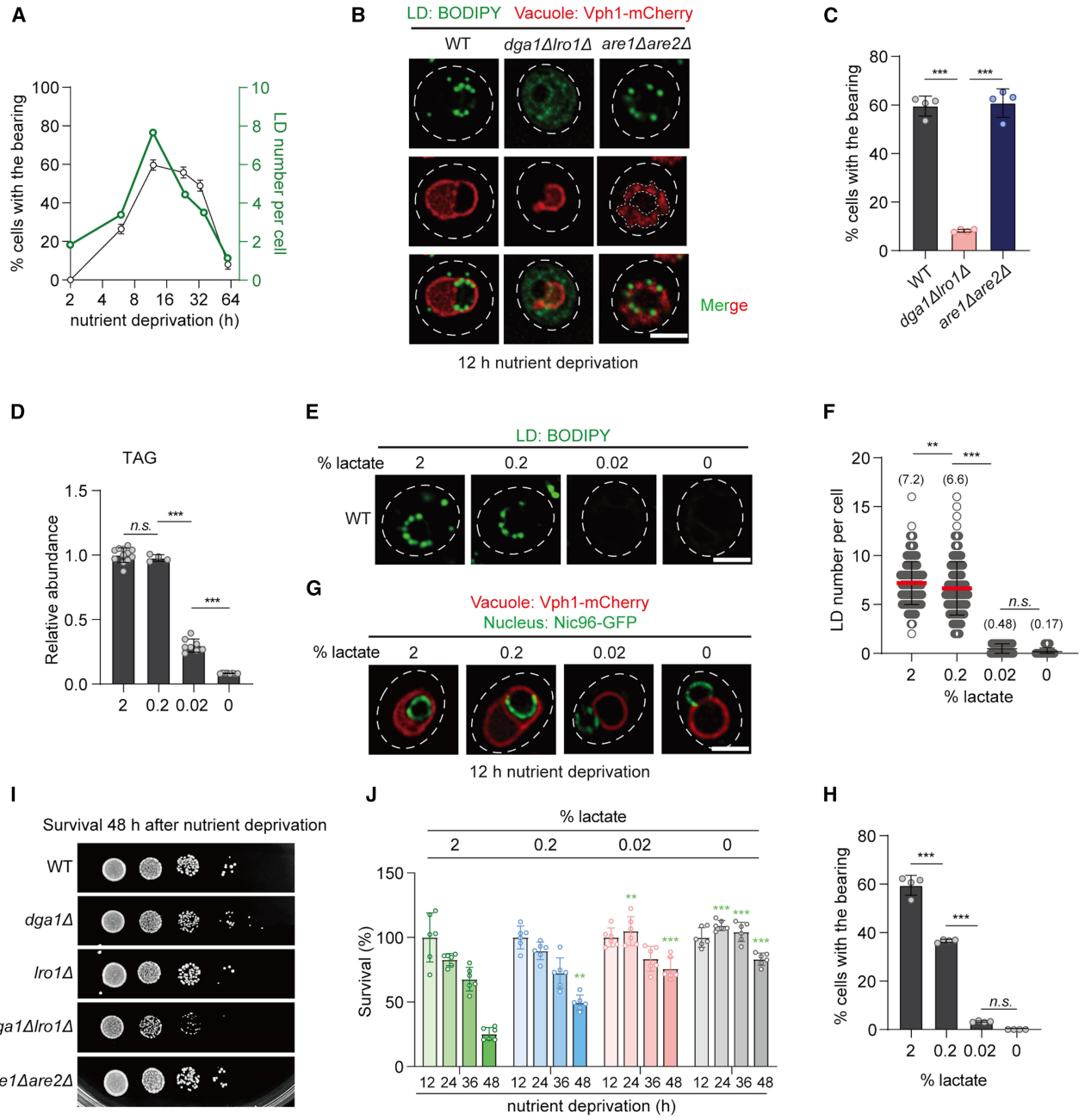

Figure 4. LD biogenesis is required for subcellular bearing formation and survival under nutrient deprivation

See also Figure S2.

(A) Quantification of WT cells with subcellular bearings at 2, 6, 12, 24, 36, and 60 h of nutrient deprivation (black) and the number of LDs in WT cells during nutrient deprivation (green). Data are represented as mean ± SD (for subcellular bearing quantification, $n = 3$ independent experiments; for LD quantification, $n = 426$, 372, 693, 297, 279, and 277 cells).

(B) Live cell imaging of cells labeled with Vph1-mCherry (vacuoles) and BODIPY (LDs) after 12 h of nutrient deprivation. Scale bar, 2 μm.

(C) Quantification of subcellular bearings. Data are represented as mean ± SD ($n = 4$ independent experiments with >200 cells quantified per condition). *** $p < 0.001$.

(D) Relative TAG levels. Data are represented as mean ± SD (for each lactate concentration, $n = 12$, 4, 8, and 8 respectively from left to right; biologically independent samples). *** $p < 0.001$; n.s., no significance.

(E) BODIPY staining of LDs in WT cells after 12 h of nutrient deprivation with varying lactate concentrations. Scale bar, 2 μm.

(F) Quantification of LD numbers in WT cells under the conditions as (E). Data shown are representative of experiments repeated twice and represented as mean ± SD (for each lactate concentration, $n = 233$, 177, 256, and 256 cells). ** $p < 0.01$; *** $p < 0.001$; n.s., no significance.

(G) Live cell imaging of vacuoles with Vph1-mCherry and the nucleus with Nic96-GFP. Scale bar, 2 μm.

(legend continued on next page)

for LDs). During the time-lapse imaging, we observed LDs moving along the nuclear periphery, occasionally undergoing fusion (Figures S2G and S2H, Video S3). Concurrently, the NVJ also exhibited dynamic behavior, with Nvj1-GFP showing variations in intensity and length over the 1-h tracking period (Figures S2G and S2H, Video S3). These dynamic patterns and the temporal evidence suggest a causative role of LDs in NVJ extension, which consequently promotes subcellular bearing formation.

To test this hypothesis, we next measured NVJ length in cells where LD biogenesis was restricted by blocking TAG production, either using the *dga1Δlro1Δ* mutant or by reducing exogenous lactate concentration during nutrient deprivation. In the LD-deficient *dga1Δlro1Δ* mutant, the average NVJ length was significantly reduced 12 h after nutrient deprivation compared with WT cells (Figures 5E and 5F). Interestingly, the additional elimination of ergosterol ester synthesis (*are1Δare2Δ*) in the TAG-deficient mutant (*dga1Δlro1Δ*) resulted in NVJ fragmentation (Figures 5G and 5H). This fragmentation was also observed in the *are1Δare2Δ* mutant (Figures 5G and 5H), suggesting that the lack of sterol esterification underlies this phenotype. The observed NVJ fragmentation is likely attributed to nuclear ER interactions with multiple small vacuoles that surround and interact with the nuclear ER (Figures 5I and 5J). It seems that the inhibition of ergosterol esterification impairs vacuole fusion, preventing the formation of a single, enlarged vacuole.

Similarly, diminishing lactate to restrict LD biogenesis also led to reduced NVJ length (Figure 5K), with approximately 58% and 72% decreases observed in 0.02% and 0% lactate, respectively, after 12 h of nutrient deprivation (Figure 5L). However, NVJs were still able to extend in these LD-deficient cells, although less effectively compared with WT cells or those with sufficient lactate supporting LD production (Figures 5F and 5L). Taken together, these findings indicate that LD biogenesis is not essential for NVJ extension, but facilitates the process and subsequently subcellular bearing formation.

We further investigated whether the absence of choline in minimal medium is a contributing factor to subcellular bearing formation, as choline deficiency can limit phosphatidylcholine biosynthesis and affect cell growth.[38] Cells were supplemented with 1 mM choline under nutrient deprivation and analyzed 12 h later. We observed no significant changes in LD numbers (Figure S2I), NVJ length (Figure S2J), or the percentage of cells displaying subcellular bearings (Figure S2K). These findings indicate that exogenous choline does not affect subcellular bearing formation.

The vacuole receptor protein Vac8 is essential for subcellular bearing formation by tethering vCLIP and NVJ contacts

To further dissect the molecular machinery required for this LD-bridged formation of subcellular bearings, we visualized other component proteins Osh1, Mdm1, and Vac8 at the NVJ[39–41] (Figure 5A). All three proteins displayed concentrated GFP signals at these junctions, which extended during 12 h of nutrient deprivation (Figure S3A). Deletion of *NVJ1*, *MDM1*, or both significantly reduced subcellular bearing formation (Figures 6A and 6B). Consistently, the deletion of *SND3*, encoding an ER protein crucial for NVJ formation,[42] inhibited NVJ extension (Figures S3B and S3C) and disrupted subcellular bearing formation under nutrient deprivation (Figures S3D and S3E). Interestingly, deletion of the vacuole receptor protein Vac8 completely abolished subcellular bearing formation (Figure 6B), underlying an essential role of Vac8 in forming this organelle triad.

Given the established interactions of Vac8 with Nvj1 for NVJ formation[41,43] and with LDO proteins for the vacuole-LD contact site vCLIP formation[44,45] (Figure 6C), we investigated whether vCLIP formation plays a crucial role in LD-mediated NVJ extension and subcellular bearing formation. Acknowledging the potential for heterogeneous LDO distribution across LDs,[46] we visualized LDO localization by chromosomally tagging Ldo16 with mCherry and Erg6 with GFP at the C terminus. Because LDO proteins are encoded by overlapping genes,[46] this tagging allows us to simultaneously visualize both proteins. Under lactate-based nutrient deprivation conditions, Ldo16/45 predominantly colocalized with nearly all LDs (Figure S3F). The genetic disruption of *LDO16* and *LDO45* led to vCLIP disruption, evidenced by fewer LD-vacuole contacts (Figure 6D), and a substantial reduction in subcellular bearing formation (<20%) (Figures 6D and 6E), a more pronounced effect than *nvj1Δ* (Figure 6B). Strikingly, the triple mutant *nvj1Δldo16Δldo45Δ* completely abolished subcellular bearing formation (Figures 6F and 6G), mirroring the *vac8Δ* phenotype (Figure 6B). These genetic data strongly suggest that vCLIP and NVJ, mediated by LDO-Vac8 and Nvj1-Vac8 interactions, respectively, are the necessary contacts for subcellular bearing formation.

LD biogenesis promotes NVJ extension by coupling vCLIP formation

Next, we tracked the localization of LDO proteins and Vac8 during 12-h nutrient deprivation period. Concomitant with increasing LD numbers, we observed a progressive concentration of Vac8 at the NVJ side of the vacuole, accompanied by a decrease in Vac8-associated LDs between 6 and 12 h (Figure 6H and see quantification in Figure S3G). Notably, early LDs (2 h) exhibited high colocalization with Vac8 (Figures 6H and S3G). This temporal pattern suggests that LD biogenesis contributes to Vac8-mediated NVJ extension, likely through vCLIP formation. We propose that LDO-Vac8 interaction during vCLIP formation concentrates Vac8 at the ONM-facing vacuolar membrane, providing a spatial advantage for Nvj1-Vac8 interaction and subsequent NVJ extension. To test this, we deleted *NVJ1* and LDO proteins, examining their effects on Vac8 localization. As predicted, LDs did not colocalize with Vac8-mCherry in the absence of LDO proteins (Figures 6I and S3H),

(H) Quantification of subcellular bearing formation. Data are represented as mean ± SD (n = 4 independent experiments with >200 cells quantified per condition). *** $p < 0.001$; n.s., no significance.

(I) Spotting assaying survival after 48 h of nutrient deprivation.

(J) Relative survival rates. Data are represented as mean ± SD (n = 6 biologically independent samples). ** $p < 0.01$; *** $p < 0.001$. Green asterisks indicate statistical significance for comparisons between 2% lactate and each respective lactate concentration at the same time point.

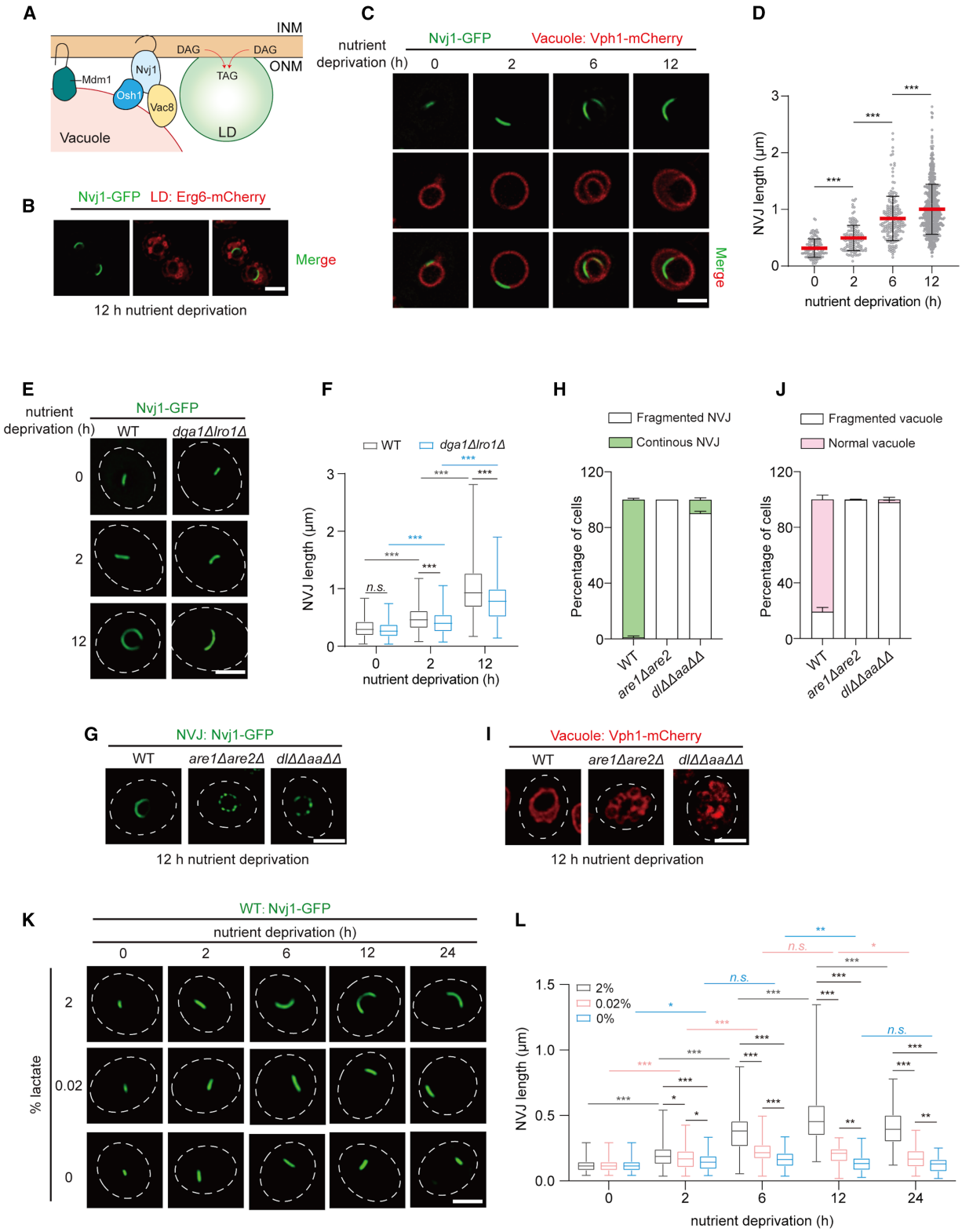

Figure 5. LDs promote NVJ extension during subcellular bearing formation

See also Video S3.

(A) Schematic representation of NVJ and LD biogenesis.

(legend continued on next page)

confirming the role of LDO proteins in tethering LDs to the vacuole via Vac8.[44,45] Intriguingly, in the absence of Nvj1 interaction (*nvj1Δ*), Vac8-mCherry signals concentrated near LDs (Figures 6I and S3H).

We further tested whether LDO expression affect NVJ extension by deleting LDO proteins or overexpressing *LDO16*. Consistent with LD biogenesis limiting NVJ extension, cells lacking LDO proteins exhibited defective NVJ extension (Figures 6J and 6K), highlighting a requirement for the LDO-Vac8 interaction in this process. This contrasts with previous observations during glucose deprivation, where LDO protein loss caused a slight NVJ increase.[44] These differing results suggest that metabolic states can modulate the function of Vac8's interacting partners, potentially through changes in Vac8 availability. Interestingly, the overexpression of *LDO16* also substantially reduced NVJ length at 12 h of nutrient deprivation (Figures 6J and 6K), likely due to excessive LDO-Vac8 interactions outcompeting Nvj1 binding. Taken together, our findings suggest that increased LDO-Vac8 interaction, coupled with LD biogenesis during nutrient deprivation, positions Vac8 concentrated at vacuolar membrane in close proximity to Nvj1, establishing Nvj1-Vac8 interactions for NVJ and thereby facilitating organelle triad formation.

Finally, to reinforce the importance of appropriate expression levels of the contact site proteins Vac8, Nvj1, and LDO for subcellular bearing formation, we examined their protein levels under nutrient deprivation with different carbon sources. Nvj1 protein levels significantly increased under glucose nutrient deprivation conditions, Vac8 and Ldo45 remained relatively low (Figure 6L). In contrast, under lactate nutrient deprivation, Vac8 levels significantly increased, accompanied by higher inductions of Nvj1 and Ldo45 expression (Figure 6L). This coordinated abundance of Vac8, Nvj1, and Ldo45, not observed under glucose, ethanol, or glycerol conditions (Figure 6L), seemed to be crucial for vCLIP and NVJ assembly and subcellular bearing formation.

Subcellular bearings facilitate efficient LD turnover and adaptation to nutrient stress

The formation and disassembly of subcellular bearings occur concurrently with the life cycle of LDs during prolonged 60-h nutrient deprivation (Figure 4A). As LDs grow in the ER before turning over in the vacuole, those encapsulated within subcellular bearings—situated between the nuclear ER and vacuole membranes—presumably gain a spatiotemporal advantage that streamlines their life cycle. This spatial confinement likely optimizes metabolic control over lipid deposition and use, enhancing cellular adaptation to lactate-based nutrient deprivation conditions.

To test this, we monitored LDs during prolonged nutrient deprivation in mutants that disrupt subcellular bearing formation, including *nvj1Δ*, *mdm1Δ*, *ldo16Δ*, *ldo45Δ*, *nvj1Δldo16Δldo45Δ*, *vac8Δ*, *ldo16Δldo45Δ*, and *nvj1Δmdm1Δ*. After the first 12 h of nutrient deprivation, deletion of *NVJ1* and/or *MDM1* had little impact on LD numbers (Figure S4A), while deletion of LDO proteins caused marginal reductions (Figure S4B). Notably, the *vac8Δ* and *nvj1Δldo16Δldo45Δ* mutants reduced the average LD count from 7.4 to 5.9 (Figures S4A and S4B). These findings suggest a potential role of vCLIP in LD biogenesis, while further mechanistic studies are needed to fully understand this relationship. After 24 h of nutrient deprivation, however, LD numbers in the mutants with defective subcellular bearing formation remained largely unchanged and were relatively larger in size (Figures 7A–7C and S4C–S4E). These mutants exhibited an average of more than four LDs even after 60 h of nutrient deprivation (Figures 7B and S4D). This contrasted with the gradual reduction in LD numbers and sizes observed in WT cells (Figures 7B, 7C, S4D, and S4E) and demonstrate that LD turnover was less efficient when subcellular bearing formation was impaired. This impaired LD turnover was consistent with EM observations (Figure S5A).

To investigate if lipophagy contributes to LD turnover, we performed the GFP cleavage assay using Erg6-GFP. Notably, Erg6-GFP was primarily localized to the ER before nutrient deprivation and colocalized with LDs stained with AUTODOT (Figure S5B). The GFP cleavage assay revealed that lipophagy was indeed attenuated in the subcellular bearing-defective mutants *ldo16Δldo45Δ* and *nvj1Δmdm1Δ*, which disrupt vCLIP and NVJ contact sites (Figure S5C).

The difference in LD numbers is likely driven by their catabolism to support energy metabolism required for cell survival under nutrient deprivation. Interestingly, during the first 48 h of nutrient deprivation, there were no significant differences in survivability between WT cells and mutants with disrupted subcellular bearing formation, including *vac8Δ*, *nvj1Δ*, *nvj1Δmdm1Δ*, *ldo16Δldo45Δ*, and *ldo16Δldo45Δnvj1Δ* (Figure 7D). The

(B) Live cell imaging of the NVJ labeled with Nvj1-GFP and LDs labeled with Erg6-mCherry in WT cells. Scale bar, 2 μm.
(C) Live cell imaging of the NVJ labeled with Nvj1-GFP and vacuoles labeled with Vph1-mCherry in WT cells during nutrient deprivation. Scale bar, 2 μm.
(D) Quantification of NVJ length. Data shown are representative of experiments repeated twice and represented as mean ± SD (n = 134, 153, 196, and 371 cells). *** $p < 0.001$.
(E) Live-cell imaging of the NVJ (Nvj1-GFP) in WT and *dga1Δlro1Δ* cells during nutrient deprivation. Scale bar, 2 μm.
(F) Quantification of NVJ length using Nvj1-GFP. Data shown are representative of experiments repeated twice and represented as mean ± SD (n = 132, 151, 614 for WT, n = 192, 282, and 295 for *dga1Δlro1Δ*; n = number of cells). *** $p < 0.001$; n.s., no significance.
(G) Live cell imaging of NVJ (Nvj1-GFP) in cells after 12 h of nutrient deprivation. Scale bar, 2 μm.
(H) Quantification of fragmented NVJ in (G). Data shown are representative of experiments repeated three times and represented as mean ± SD.
(I) Live cell imaging of vacuoles (Vph1-mCherry) in cells after 12 h of nutrient deprivation. Scale bar, 2 μm.
(J) Quantification of fragmented vacuoles in (I). Data shown are representative of experiments repeated three times and represented as mean ± SD.
(K) Live cell imaging of the NVJ (Nvj1-GFP) in WT cells during nutrient deprivation with varying concentrations of lactate. Scale bar, 2 μm.
(L) Quantification of NVJ length using Nvj1-GFP. Data shown are representative of experiments repeated twice and represented as mean ± SD (n = 108, 102, 112, 98, and 95 in 0% lactate, n = 108, 166, 185, 141, and 140 in 0.02% lactate, and n = 108, 205, 207, 170, and 208 in 2% lactate; n = number of cells). * $p < 0.05$; ** $p < 0.01$; *** $p < 0.001$; n.s., no significance.

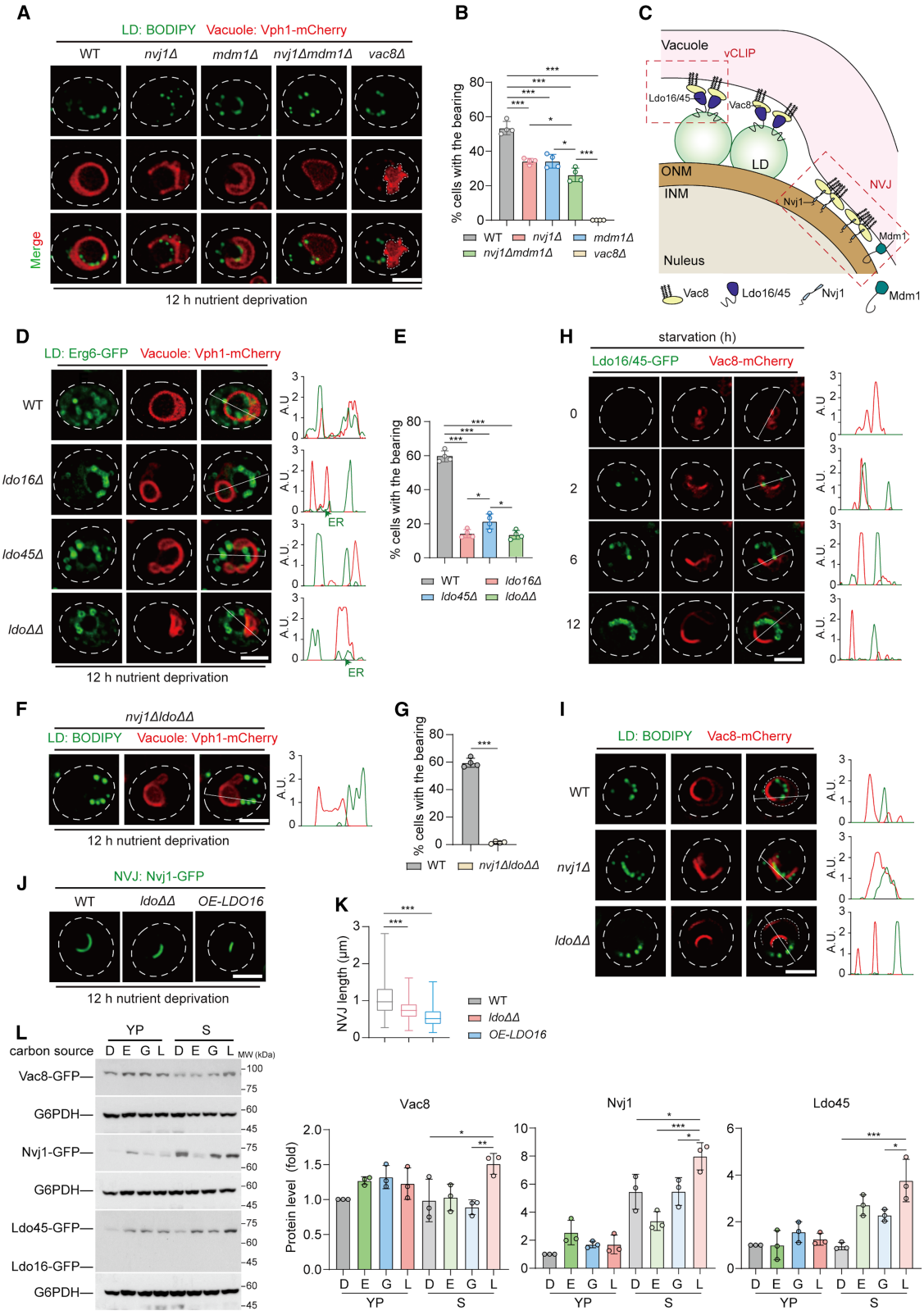

(legend on next page)

reduction in LD numbers observed among WT and these mutant cells during the first 12–24 h of nutrient deprivation was likely sufficient to meet the initial energy demands. However, after 60 h, a stark contrast emerged: all these mutants exhibited severe survival defects, while WT cells continued to survive (Figures 7D and S6A). During this later phase of nutrient deprivation, continuous LD consumption to support stress defense appears crucial, as the deficiencies in subcellular bearing formation, associated with decreased lipophagy, led to profoundly compromised cell survival.

Notably, *vac8Δ* mutants showed a strong bearing defect but survived comparatively better than other component mutants, although not at prolonged nutrient deprivation of 84 h (Figure 7D). The extent of viability defects did not perfectly match the efficiency of bearing formation. This discrepancy could reflect the multifunctional nature of Vac8 and the compromised growth rate of the *vac8Δ* mutant (Figure S6B). It is plausible that the slow-growing strain may experience less severe metabolic stress under nutrient deprivation.

We also found that the *sei1Δ* mutant, which exhibited disrupted subcellular bearing formation (Figure S2E), also displayed reduced survival (Figure S6C). A mutant with normal bearing formation but excessive nuclear ER formation (due to overexpression of *PCT1*, the rate-limiting enzyme in the Kennedy pathway for PC synthesis) maintained normal survival rates (Figures S6D–S6F). These findings further support the critical role of subcellular bearing formation in survival under nutrient deprivation.

We next conducted survival experiments by overexpressing *MDM1* in the *nvj1Δ* mutant, *NVJ1* in the *ldo16Δldo45Δ* mutant, and *LDO16* in the *nvj1Δmdm1Δ* mutant. Overexpression of *NVJ1* and *LDO16* improved survival of the *ldo16Δldo45Δ* and *nvj1Δmdm1Δ* mutants under prolonged nutrient deprivation, respectively, but *MDM1* overexpression did not rescue the survival defect in the *nvj1Δ* mutant (Figure 7E). These results suggest that the expression of alternative tethering proteins can compensate for specific gene deletions, and that defective bearing formation is a key factor contributing to survival defects under prolonged nutrient deprivation.

DISCUSSION

In this study, we report a bearing-like subcellular organization of cell organelles in budding yeast as an adaptive response to nutrient stress. As illustrated in Figure 7F, subcellular bearings are an organelle triad, where the vacuole expands and deforms into a crescent shape, wrapping around the nucleus attached with an orbit of LDs. This dynamic and transient structural integration occurs in parallel with LD biogenesis and turnover. The rapid production of LDs from the nuclear ER under nutrient deprivation in the presence of lactate facilitates the tethering of the vacuole through Vac8-LDO interactions at vCLIP contact sites, which further promotes Vac8/Nvj1-dependent NVJ extension. Formation of this subcellular bearing structure is crucial for the timely utilization of LDs, which likely fuels energy metabolism required for cell survival during prolonged nutrient deprivation.

Interestingly, the formation of subcellular bearings under nutrient deprivation seems to be specific to conditions with excess lactate, although it can also be observed in the presence of glycerol (Figure S1G). This specificity seems to be linked to the coordinated upregulation of proteins crucial for vCLIP and NVJ formation, namely Vac8, Nvj1, and LDO (Figure 6L). These proteins exhibit significantly higher expression levels under lactate conditions compared with glucose, ethanol, or glycerol. This coordinated increase, coupled with a surge in LD biogenesis, creates a unique cellular context that promotes triad formation. The organelle triad formation, as a cellular strategy for managing nutrient stress, likely corresponds to the severity of the stress. For example, cells continued to grow after switching from rich medium to minimal medium with ethanol, whereas growth readily halted in the presence of glycerol or lactate (Figure 1B). This growth phenotype suggests that different non-fermentable carbon sources can induce varying levels of metabolic stress. Under ethanol conditions, LDs were generated and increased in size over 24 h of nutrient deprivation, while under lactate conditions, LD numbers peaked at 12 h of nutrient deprivation and then decreased in size (Figures S1E and S1F). The changes in LDs

Figure 6. Vac8-mediated vCLIP and NVJ contacts are critical for the formation of subcellular bearing structures

See also Figure S3.

(A) Live cell imaging of LDs stained with BODIPY and the vacuole labeled with Vph1-mCherry in cells after 12 h of nutrient deprivation. Scale bar, 2 μm.

(B) Quantification of subcellular bearing formation. Data are represented as mean ± SD ($n = 4$ independent experiments; >200 cells were quantified). * $p < 0.05$; *** $p < 0.001$.

(C) Schematic representation of NVJ (Nvj1-Vac8 complex and Mdm1) and vCLIP (Ldo16/45-Vac8 complex).

(D) Live cell imaging of LDs (Erg6-GFP) and the vacuole (Vph1-mCherry). Scale bar, 2 μm. Fluorescence intensity was measured across a line spanning the vacuole and LDs. A.U., arbitrary fluorescence units.

(E) Quantification of subcellular bearing formation. Data are represented as mean ± SD ($n = 4$ independent experiments; >200 cells were quantified). * $p < 0.05$ ***, $p < 0.001$.

(F) Live cell imaging of LDs stained with BODIPY and the vacuole labeled with Vph1-mCherry in *nvj1Δldo16Δldo45Δ* (*nvj1ΔldoΔ*Δ) cells. Scale bar, 2 μm. Fluorescence intensity was measured across a line spanning the vacuole and LDs. A.U., arbitrary fluorescence units.

(G) Quantification of subcellular bearing formation. Data are represented as mean ± SD ($n = 4$ independent experiments; >200 cells were quantified). *** $p < 0.001$.

(H) Live cell imaging of Ldo16/45-GFP and Vac8-mCherry. Scale bar, 2 μm. Fluorescence intensity was measured across a line spanning the Vac8 and LDO proteins.

(I) Live-cell imaging of LDs stained with BODIPY and Vac8-mCherry. Scale bar, 2 μm. Fluorescence intensity was measured across a line spanning LDs and Vac8.

(J) Live cell imaging of NVJ (Nvj1-GFP). Scale bar, 2 μm.

(K) Quantification of NVJ length. Data are represented as mean ± SD ($n = 245$ for WT, 257 for *ldo16Δldo45Δ*; 247 for *OE-LDO16*; n = number of cells). *** $p < 0.001$.

(L) Western blots showing Vac8, Nvj1, and Ldo45 protein levels under nutrient deprivation conditions with various carbon sources. Data are representative of three independent experiments and are presented as mean ± SD. * $p < 0.05$; ** $p < 0.01$; *** $p < 0.001$.

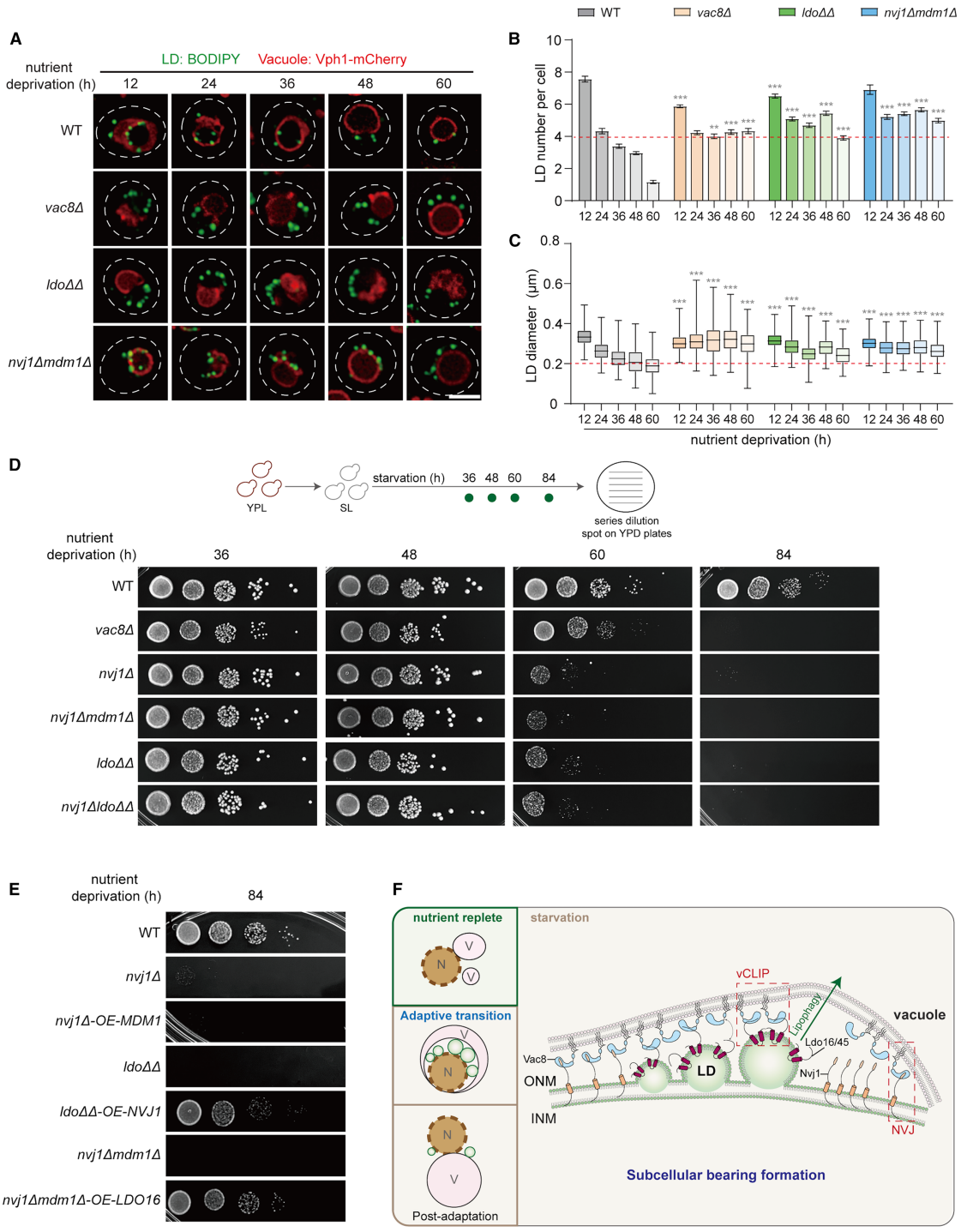

Figure 7. Subcellular bearings facilitate efficient LD turnover and adaptation to nutrient stress

See also Figures S4–S6.

(A) Live cell imaging of LDs stained with BODIPY and the vacuole labeled with Vph1-mCherry. Scale bar, 2 μm.

(B) Quantification of LD numbers. Data shown are representative of experiments repeated twice and are represented as mean ± SD (n = 138, 174, 154, 256, and 242 for WT, n = 403, 256, 164, 168, and 155 for *vac8Δ*, n = 212, 256, 232, 256, and 232 for *ldo16Δldo45Δ*, and n = 254, 202, 253, 251, and 230 for *nvj1Δmdm1Δ*; n = number of cells). ** $p < 0.01$; *** $p < 0.001$. Gray asterisks indicate statistical significance for comparisons between WT and the mutant cells at the same time point.

(legend continued on next page)

under different stress conditions indicate that lipid deposition and use are critical mechanisms for cellular adaptation. While we do not fully understand why lactate specifically induces toxic effects under this condition, we speculate that it may be due to excessive fatty acid production. If not efficiently sequestered into LDs, these fatty acids could disrupt intracellular membrane integrity, leading to toxicity.

Recent studies have shown that LDO proteins residing on LDs ensure their vacuole targeting by interacting with Vac8, facilitating their subsequent turnover through lipophagy at the vacuole.[44,45] Consistent with this, Vac8-mediated vCLIP contact sites were found to be essential for both subcellular bearing formation and LD turnover. Our findings further demonstrate that disrupting LDO protein expression—either through depletion or overexpression—can impair NVJ extension, a process dependent on Vac8-Nvj1 interactions.[41–43] Our findings suggest that LDO-mediated LD tethering to the vacuole, while necessary for expanding the vacuole-nuclear ER interface, requires precise regulation. We propose that LD growth at the nuclear ER enhances LDO protein interaction with the vacuole receptor protein Vac8, forming vCLIP contacts (Figure 7F). Such increases in Vac8 concentrations at the vacuolar membrane facing the ONM likely facilitate Nvj1-Vac8 interactions, driving NVJ formation. Thus, LD biogenesis promotes NVJ extension via increased vCLIP formation, leading to subcellular bearing formation (Figure 7F). These membrane tethers deform the vacuole as it interacts with both LDs and the nuclear ER. Conversely, LD shrinkage via turnover processes such as lipophagy during prolonged nutrient deprivation results in subcellular bearing disassembly, as LDs become insufficient to maintain vCLIP contacts and thus limit NVJ establishment. In summary, we uncover a subcellular organizational principle enabling cells to adapt to severe nutrient stress. This mechanism autonomously optimizes lipid deposition and utilization, based on LD size and number, through membrane contacts with the nuclear ER and vacuole.

Limitations of the study

This study reveals an extreme remodeling of organelle organization, culminating in a triad structure under nutrient deprivation, yet mechanistic gaps remain. Specifically, we have not fully resolved how LDO-Vac8-mediated vCLIP and Nvj1-Vac8-mediated NVJ interactions drive the physical assembly of LDs, the vacuole, and the nuclear ER into the subcellular bearing structure. Furthermore, the roles of Sei1 and LDO proteins in LD biogenesis and subcellular bearing formation under this nutrient deprivation condition require further exploration. Understanding the full complement of components and regulatory mechanisms involved in subcellular bearing formation necessitates additional research.

RESOURCE AVAILABILITY

Lead contact

Further information and requests for resources and reagents should be directed to and will be fulfilled by the lead contact, Cunqi Ye (yecunqi@zju.edu.cn).

Materials availability

All the yeast strains generated in this study are available upon request.

Data and code availability

- All data reported in this paper will be shared by the lead contact upon request.
- This paper does not report original code.
- Original western blot images have been deposited at Mendeley Data and are publicly available. Accession numbers are listed in the key resources table.
- Any additional information required to reanalyze the data reported in this paper is available from the lead contact upon request.

ACKNOWLEDGMENTS

We thank Jiatian Mu, Tong Zhang, and Kunpeng Zhou from the Ye laboratory for helping strain construction; Xueying Jiang from the Core Facility of Life Sciences Institute of Zhejiang University; Li Xie from Analysis Center of Agrobiology and Environmental Sciences of Zhejiang University; and Jiansheng Guo from Center of Cryo-Electron Microscopy, Zhejiang University School of Medicine for their technical support. This work was supported by grants from the National Key Research and Development Program of China (2024YFA1803000 and 2023YFA1801100), the National Natural Science Foundation of China (32270816 and 92057102), Double Thousand Plan of Jiangxi Province (jxsq2023102239), the Fundamental Research Funds for the Central Universities (226-2024-00088), the startup fund from the Life Sciences Institute of Zhejiang University, and the 1000 Talents Program for Young Scholars to C.Y.

AUTHOR CONTRIBUTIONS

Conceptualization, C.Y., H.Q., and C.M.; investigation, H.Q., C.M., and C.Y.; supervision, C.Y.; writing and funding acquisition, C.Y.

DECLARATION OF INTERESTS

The authors declare no competing interests.

STAR★METHODS

Detailed methods are provided in the online version of this paper and include the following:

- KEY RESOURCES TABLE
- EXPERIMENTAL MODEL AND SUBJECT DETAILS
- METHOD DETAILS
  - Transmission electronic microscopy (TEM) imaging
  - Electron tomography (ET) and 3D reconstruction
  - 3D imaging of a subcellular bearing using FIB-SEM
  - 3D reconstruction using spinning disk confocal microscopy and Imaris
  - Live cell imaging

(C) Quantification of LD diameters. Data are represented as mean ± SD (n = 238, 256, 212, 238, and 231 for WT, n = 250, 230, 253, 252, and 251 for *vac8Δ*, n = 229, 221, 237, 229, and 228 for *ldo16Δldo45Δ*, and n = 233, 220, 231, 205, and 219 for *nvj1Δmdm1Δ*; n = number of cells). *** $p < 0.001$. Gray asterisks indicate statistical significance for comparisons between WT and the mutant cells at the same time point.
(D) Survival of cells after nutrient deprivation.
(E) Survival of cells after 84 h of nutrient deprivation.
(F) Models depicting the formation of subcellular bearings under nutrient deprivation.

SUPPLEMENTAL INFORMATION

Supplemental information can be found online at https://doi.org/10.1016/j.celrep.2025.115813.

Received: November 27, 2024
Revised: April 3, 2025
Accepted: May 20, 2025

REFERENCES

1. Manning, B.D. (2013). Adaptation to starvation: translating a matter of life or death. Cancer Cell *23*, 713–715. https://doi.org/10.1016/j.ccr.2013.05.012.
2. Palm, W., and Thompson, C.B. (2017). Nutrient acquisition strategies of mammalian cells. Nature *546*, 234–242. https://doi.org/10.1038/nature22379.
3. Cai, L., and Tu, B.P. (2012). Driving the cell cycle through metabolism. Annu. Rev. Cell Dev. Biol. *28*, 59–87. https://doi.org/10.1146/annurev-cellbio-092910-154010.
4. Walsh, C.T., Tu, B.P., and Tang, Y. (2018). Eight Kinetically Stable but Thermodynamically Activated Molecules that Power Cell Metabolism. Chem. Rev. *118*, 1460–1494. https://doi.org/10.1021/acs.chemrev.7b00510.
5. Ye, C., and Tu, B.P. (2018). Sink into the Epigenome: Histones as Repositories That Influence Cellular Metabolism. Trends Endocrinol. Metab. *29*, 626–637. https://doi.org/10.1016/j.tem.2018.06.002.
6. Youle, R.J., and Narendra, D.P. (2011). Mechanisms of mitophagy. Nat. Rev. Mol. Cell Biol. *12*, 9–14. https://doi.org/10.1038/nrm3028.
7. Walther, T.C., and Farese, R.V., Jr. (2012). Lipid droplets and cellular lipid metabolism. Annu. Rev. Biochem. *81*, 687–714. https://doi.org/10.1146/annurev-biochem-061009-102430.
8. Rogers, S., Gui, L., Kovalenko, A., Zoni, V., Carpentier, M., Ramji, K., Ben Mbarek, K., Bacle, A., Fuchs, P., Campomanes, P., et al. (2022). Triglyceride lipolysis triggers liquid crystalline phases in lipid droplets and alters the LD proteome. J. Cell Biol. *221*, e202205053. https://doi.org/10.1083/jcb.202205053.
9. Korolchuk, V.I., Saiki, S., Lichtenberg, M., Siddiqi, F.H., Roberts, E.A., Imarisio, S., Jahreiss, L., Sarkar, S., Futter, M., Menzies, F.M., et al. (2011). Lysosomal positioning coordinates cellular nutrient responses. Nat. Cell Biol. *13*, 453–460. https://doi.org/10.1038/ncb2204.
10. Lu, M., van Tartwijk, F.W., Lin, J.Q., Nijenhuis, W., Parutto, P., Fantham, M., Christensen, C.N., Avezov, E., Holt, C.E., Tunnacliffe, A., et al. (2020). The structure and global distribution of the endoplasmic reticulum network are actively regulated by lysosomes. Sci. Adv. *6*, eabc7209. https://doi.org/10.1126/sciadv.abc7209.
11. Bar-Peled, L., and Kory, N. (2022). Principles and functions of metabolic compartmentalization. Nat. Metab. *4*, 1232–1244. https://doi.org/10.1038/s42255-022-00645-2.
12. Scorrano, L., De Matteis, M.A., Emr, S., Giordano, F., Hajnóczky, G., Kornmann, B., Lackner, L.L., Levine, T.P., Pellegrini, L., Reinisch, K., et al. (2019). Coming together to define membrane contact sites. Nat. Commun. *10*, 1287. https://doi.org/10.1038/s41467-019-09253-3.
13. Prinz, W.A., Toulmay, A., and Balla, T. (2020). The functional universe of membrane contact sites. Nat. Rev. Mol. Cell Biol. *21*, 7–24. https://doi.org/10.1038/s41580-019-0180-9.
14. Lahiri, S., Toulmay, A., and Prinz, W.A. (2015). Membrane contact sites, gateways for lipid homeostasis. Curr. Opin. Cell Biol. *33*, 82–87. https://doi.org/10.1016/j.ceb.2014.12.004.
15. Bravo-Sagua, R., Torrealba, N., Paredes, F., Morales, P.E., Pennanen, C., López-Crisosto, C., Troncoso, R., Criollo, A., Chiong, M., Hill, J.A., et al. (2014). Organelle communication: signaling crossroads between homeostasis and disease. Int. J. Biochem. Cell Biol. *50*, 55–59. https://doi.org/10.1016/j.biocel.2014.01.019.
16. Voeltz, G.K., Sawyer, E.M., Hajnóczky, G., and Prinz, W.A. (2024). Making the connection: How membrane contact sites have changed our view of organelle biology. Cell *187*, 257–270. https://doi.org/10.1016/j.cell.2023.11.040.
17. Brooks, G.A. (2020). Lactate as a fulcrum of metabolism. Redox Biol. *35*, 101454. https://doi.org/10.1016/j.redox.2020.101454.
18. Brooks, G.A. (2018). The Science and Translation of Lactate Shuttle Theory. Cell Metab. *27*, 757–785. https://doi.org/10.1016/j.cmet.2018.03.008.
19. Hirschhaeuser, F., Sattler, U.G.A., and Mueller-Klieser, W. (2011). Lactate: a metabolic key player in cancer. Cancer Res. *71*, 6921–6925. https://doi.org/10.1158/0008-5472.Can-11-1457.
20. Certo, M., Tsai, C.H., Pucino, V., Ho, P.C., and Mauro, C. (2021). Lactate modulation of immune responses in inflammatory versus tumour microenvironments. Nat. Rev. Immunol. *21*, 151–161. https://doi.org/10.1038/s41577-020-0406-2.
21. Wu, X., and Tu, B.P. (2011). Selective regulation of autophagy by the Iml1-Npr2-Npr3 complex in the absence of nitrogen starvation. Mol. Biol. Cell *22*, 4124–4133. https://doi.org/10.1091/mbc.E11-06-0525.
22. Sutter, B.M., Wu, X., Laxman, S., and Tu, B.P. (2013). Methionine inhibits autophagy and promotes growth by inducing the SAM-responsive methylation of PP2A. Cell *154*, 403–415. https://doi.org/10.1016/j.cell.2013.06.041.
23. Yang, Y.S., Kato, M., Wu, X., Litsios, A., Sutter, B.M., Wang, Y., Hsu, C.H., Wood, N.E., Lemoff, A., Mirzaei, H., et al. (2019). Yeast Ataxin-2 Forms an Intracellular Condensate Required for the Inhibition of TORC1 Signaling during Respiratory Growth. Cell *177*, 697–710.e17. https://doi.org/10.1016/j.cell.2019.02.043.
24. Ye, C., Sutter, B.M., Wang, Y., Kuang, Z., and Tu, B.P. (2017). A Metabolic Function for Phospholipid and Histone Methylation. Mol. Cell *66*, 180–193.e8. https://doi.org/10.1016/j.molcel.2017.02.026.
25. Ye, C., Sutter, B.M., Wang, Y., Kuang, Z., Zhao, X., Yu, Y., and Tu, B.P. (2019). Demethylation of the Protein Phosphatase PP2A Promotes Demethylation of Histones to Enable Their Function as a Methyl Group Sink. Mol. Cell *73*, 1115–1126.e6. https://doi.org/10.1016/j.molcel.2019.01.012.
26. Fang, W., Jiang, L., Zhu, Y., Yang, S., Qiu, H., Cheng, J., Liang, Q., Tu, Z.C., and Ye, C. (2023). Methionine restriction constrains lipoylation and activates mitochondria for nitrogenic synthesis of amino acids. Nat. Commun. *14*, 2504. https://doi.org/10.1038/s41467-023-38289-9.
27. Qiu, H., and Ye, C. (2025). Phospholipid Biosynthesis: An Unforeseen Modulator of Nuclear Metabolism. Biol. Cell *117*, e70002. https://doi.org/10.1111/boc.70002.
28. Nguyen, T.B., Louie, S.M., Daniele, J.R., Tran, Q., Dillin, A., Zoncu, R., Nomura, D.K., and Olzmann, J.A. (2017). DGAT1-Dependent Lipid Droplet Biogenesis Protects Mitochondrial Function during Starvation-Induced Autophagy. Dev. Cell *42*, 9–21.e5. https://doi.org/10.1016/j.devcel.2017.06.003.
29. Kvam, E., and Goldfarb, D.S. (2007). Nucleus-vacuole junctions and piecemeal microautophagy of the nucleus in S. cerevisiae. Autophagy *3*, 85–92. https://doi.org/10.4161/auto.3586.

30. Rambold, A.S., Cohen, S., and Lippincott-Schwartz, J. (2015). Fatty acid trafficking in starved cells: regulation by lipid droplet lipolysis, autophagy, and mitochondrial fusion dynamics. Dev. Cell *32*, 678–692. https://doi.org/10.1016/j.devcel.2015.01.029.

31. Fang, W., Zhu, Y., Yang, S., Tong, X., and Ye, C. (2022). Reciprocal regulation of phosphatidylcholine synthesis and H3K36 methylation programs metabolic adaptation. Cell Rep. *39*, 110672. https://doi.org/10.1016/j.celrep.2022.110672.

32. Olzmann, J.A., and Carvalho, P. (2019). Dynamics and functions of lipid droplets. Nat. Rev. Mol. Cell Biol. *20*, 137–155. https://doi.org/10.1038/s41580-018-0085-z.

33. Zadoorian, A., Du, X., and Yang, H. (2023). Lipid droplet biogenesis and functions in health and disease. Nat. Rev. Endocrinol. *19*, 443–459. https://doi.org/10.1038/s41574-023-00845-0.

34. Walther, T.C., Chung, J., and Farese, R.V., Jr. (2017). Lipid Droplet Biogenesis. Annu. Rev. Cell Dev. Biol. *33*, 491–510. https://doi.org/10.1146/annurev-cellbio-100616-060608.

35. Hariri, H., Rogers, S., Ugrankar, R., Liu, Y.L., Feathers, J.R., and Henne, W.M. (2018). Lipid droplet biogenesis is spatially coordinated at ER-vacuole contacts under nutritional stress. EMBO Rep. *19*, 57–72. https://doi.org/10.15252/embr.201744815.

36. Henne, M., Goodman, J.M., and Hariri, H. (2020). Spatial compartmentalization of lipid droplet biogenesis. Biochim. Biophys. Acta. Mol. Cell Biol. Lipids *1865*, 158499. https://doi.org/10.1016/j.bbalip.2019.07.008.

37. Hariri, H., Speer, N., Bowerman, J., Rogers, S., Fu, G., Reetz, E., Datta, S., Feathers, J.R., Ugrankar, R., Nicastro, D., and Henne, W.M. (2019). Mdm1 maintains endoplasmic reticulum homeostasis by spatially regulating lipid droplet biogenesis. J. Cell Biol. *218*, 1319–1334. https://doi.org/10.1083/jcb.201808119.

38. Boumann, H.A., Gubbens, J., Koorengevel, M.C., Oh, C.S., Martin, C.E., Heck, A.J.R., Patton-Vogt, J., Henry, S.A., de Kruijff, B., and de Kroon, A.I.P.M. (2006). Depletion of phosphatidylcholine in yeast induces shortening and increased saturation of the lipid acyl chains: evidence for regulation of intrinsic membrane curvature in a eukaryote. Mol. Biol. Cell *17*, 1006–1017. https://doi.org/10.1091/mbc.e05-04-0344.

39. Manik, M.K., Yang, H., Tong, J., and Im, Y.J. (2017). Structure of Yeast OSBP-Related Protein Osh1 Reveals Key Determinants for Lipid Transport and Protein Targeting at the Nucleus-Vacuole Junction. Structure *25*, 617–629.e3. https://doi.org/10.1016/j.str.2017.02.010.

40. Henne, W.M., Zhu, L., Balogi, Z., Stefan, C., Pleiss, J.A., and Emr, S.D. (2015). Mdm1/Snx13 is a novel ER-endolysosomal interorganelle tethering protein. J. Cell Biol. *210*, 541–551. https://doi.org/10.1083/jcb.201503088.

41. Pan, X., Roberts, P., Chen, Y., Kvam, E., Shulga, N., Huang, K., Lemmon, S., and Goldfarb, D.S. (2000). Nucleus-vacuole junctions in Saccharomyces cerevisiae are formed through the direct interaction of Vac8p with Nvj1p. Mol. Biol. Cell *11*, 2445–2457. https://doi.org/10.1091/mbc.11.7.2445.

42. Tosal-Castano, S., Peselj, C., Kohler, V., Habernig, L., Berglund, L.L., Ebrahimi, M., Vögtle, F.N., Höög, J., Andréasson, C., and Büttner, S. (2021). Snd3 controls nucleus-vacuole junctions in response to glucose signaling. Cell Rep. *34*, 108637. https://doi.org/10.1016/j.celrep.2020.108637.

43. Jeong, H., Park, J., Kim, H.I., Lee, M., Ko, Y.J., Lee, S., Jun, Y., and Lee, C. (2017). Mechanistic insight into the nucleus-vacuole junction based on the Vac8p-Nvj1p crystal structure. Proc. Natl. Acad. Sci. USA *114*, E4539–E4548. https://doi.org/10.1073/pnas.1701030114.

44. Álvarez-Guerra, I., Block, E., Broeskamp, F., Gabrijelčič, S., Infant, T., de Ory, A., Habernig, L., Andréasson, C., Levine, T.P., Höög, J.L., and Büttner, S. (2024). LDO proteins and Vac8 form a vacuole-lipid droplet contact site to enable starvation-induced lipophagy in yeast. Dev. Cell *59*, 759–775.e755. https://doi.org/10.1016/j.devcel.2024.01.014.

45. Diep, D.T.V., Collado, J., Hugenroth, M., Fausten, R.M., Percifull, L., Wälte, M., Schuberth, C., Schmidt, O., Fernández-Busnadiego, R., and Bohnert, M. (2024). A metabolically controlled contact site between vacuoles and lipid droplets in yeast. Dev. Cell *59*, 740–758.e10. https://doi.org/10.1016/j.devcel.2024.01.016.

46. Eisenberg-Bord, M., Mari, M., Weill, U., Rosenfeld-Gur, E., Moldavski, O., Castro, I.G., Soni, K.G., Harpaz, N., Levine, T.P., Futerman, A.H., et al. (2018). Identification of seipin-linked factors that act as determinants of a lipid droplet subpopulation. J. Cell Biol. *217*, 269–282. https://doi.org/10.1083/jcb.201704122.

47. van Dijken, J.P., Bauer, J., Brambilla, L., Duboc, P., Francois, J.M., Gancedo, C., Giuseppin, M., Heijnen, J.J., Hoare, M., Lange, H.C., et al. (2000). An interlaboratory comparison of physiological and genetic properties of four Saccharomyces cerevisiae strains. Enzyme Microb. Technol. *26*, 706–714. https://doi.org/10.1016/S0141-0229(00)00162-9.

48. Kremer, J.R., Mastronarde, D.N., and McIntosh, J.R. (1996). Computer visualization of three-dimensional image data using IMOD. J. Struct. Biol. *116*, 71–76. https://doi.org/10.1006/jsbi.1996.0013.

49. Longtine, M.S., McKenzie, A., 3rd, Demarini, D.J., Shah, N.G., Wach, A., Brachat, A., Philippsen, P., and Pringle, J.R. (1998). Additional modules for versatile and economical PCR-based gene deletion and modification in Saccharomyces cerevisiae. Yeast *14*, 953–961. https://doi.org/10.1002/(SICI)1097-0061(199807)14:10<953::AID-YEA293>3.0.CO;2-U.

50. Wright, R. (2000). Transmission electron microscopy of yeast. Microsc. Res. Tech. *51*, 496–510. https://doi.org/10.1002/1097-0029(20001215)51:6<496::Aid-Jemt2>3.0.Co;2-9.

51. Xie, L., Song, X.J., Liao, Z.F., Wu, B., Yang, J., Zhang, H., and Hong, J. (2019). Endoplasmic reticulum remodeling induced by Wheat yellow mosaic virus infection studied by transmission electron microscopy. Micron *120*, 80–90. https://doi.org/10.1016/j.micron.2019.01.007.

52. Fees, C.P., Estrem, C., and Moore, J.K. (2017). High-resolution Imaging and Analysis of Individual Astral Microtubule Dynamics in Budding Yeast. J. Vis. Exp. 55610. https://doi.org/10.3791/55610.

53. Yang, S., Xue, J., and Ye, C. (2022). Protocol for rapid and accurate quantification of phospholipids in yeast and mammalian systems using LC-MS. STAR Protoc. *3*, 101769. https://doi.org/10.1016/j.xpro.2022.101769.

STAR★METHODS

KEY RESOURCES TABLE

REAGENT or RESOURCE	SOURCE	IDENTIFIER
Antibodies		
Mouse anti-GFP	Roche	Cat#11814460; RRID: AB_390913
Rabbit anti-G6PDH	Sigma	Cat#A9521; RRID: AB_258454
Chemicals, Peptides, and Recombinant Proteins		
Sodium-DL-Lactate solution	Sigma	Cat#L4263
D-glucose	Sangon Biotech	Cas#50-99-7
Ethanol	Sinopharm Chemical Reagent	Cas#64-17-5
Glycerol	Sangon Biotech	Cas#56-81-5
Glutaraldehyde	Ted Pella	Cat#2171002
Osmium tetroxide	Ted Pella	Cat#4008-160501
Potassium ferrocyanide	Sigma	Cas#14459-95-1
Thiocarbohydrazide	Sigma	Cas#2231-57-4
BODIPY 493/503	Thermo Fisher Scientific	Cat#D3922
AUTODOT	Abcepta	Cat#SM1000a
Pierce BCA protein assay	Thermo Fisher Scientific	Cat#23225
Concanavalin A	Sigma	Cat#11028-71-0
Phenylmethylsulfonyl fluroride	Sigma	Cat#P7626
Potassium permanganate	YONGHUA	Cat#7722-64-7
Potassium phosphate	Sangon Biotech	Cat#7778-53-2
Sodium orthovanadate	MP Biomedicals	Cat#159664
LIPIDOMIX	Avanti Polar Lipids	Cat#330707
14:0 PS (1,2-Dimyristoyl-*sn*-glycero-3-phospho-L-serine sodium salt)	Avanti Polar Lipids	Cat#105405
17:0 PC (1,2-diheptadecanoyl-*sn*-glycero-3-phosphocholine)	Avanti Polar Lipids	Cat#70897
17:0 PE (1,2-diheptadecanoyl-*sn*-glycero-3-phosphoethanolamine)	Avanti Polar Lipids	Cat#140219
Deposited Data		
Original western blot images	This manuscript	https://doi.org/10.17632/pkjszmcsn4.1
Experimental Models: Organisms/Strains		
S. cerevisiae: Name = CEN.PK; Genotype = MATa	Van Dijken et al.[47]	N/A
S. cerevisiae: Name = CEN.PK; Genotype = MATa; NIC96-GFP::NAT; VPH1-mCherry:KanMX	This manuscript	N/A
S. cerevisiae: Name = CEN.PK; Genotype = MATa; VPH1-GFP::HYG	This manuscript	N/A
S. cerevisiae: Name = CEN.PK; Genotype = MATa; ERG6-GFP::NAT	This manuscript	N/A
S. cerevisiae: Name = CEN.PK; Genotype = MATa; DPM1-GFP::HYG	This manuscript	N/A
S. cerevisiae: Name = CEN.PK; Genotype = MATa; OM45-GFP::NAT	This manuscript	N/A
S. cerevisiae: Name = CEN.PK; Genotype = MATa; PEX3-GFP::HYG	This manuscript	N/A
S. cerevisiae: Name = CEN.PK; Genotype = MATa; NUP60-NLS-CFP::HYG; VPH1-mCherry:NAT	This manuscript	N/A
S. cerevisiae: Name = CEN.PK; Genotype = MATa; dga1Δ::HYG; lro1Δ::NAT; VPH1-mCherry:KanMX	This manuscript	N/A

(*Continued on next page*)

Continued

REAGENT or RESOURCE	SOURCE	IDENTIFIER
S. cerevisiae: Name = CEN.PK; Genotype = MATa; are1Δ::NAT; are2Δ::HYG; VPH1-mCherry:KanMX	This manuscript	N/A
S. cerevisiae: Name = CEN.PK; Genotype = MATa; dga1Δ::HYG; lro1Δ::NAT	This manuscript	N/A
S. cerevisiae: Name = CEN.PK; Genotype = MATa; are1Δ::NAT; are2Δ::HYG	This manuscript	N/A
S. cerevisiae: Name = CEN.PK; Genotype = MATa; dga1Δ::NAT	This manuscript	N/A
S. cerevisiae: Name = CEN.PK; Genotype = MATa; lro1Δ::NAT	This manuscript	N/A
S. cerevisiae: Name = CEN.PK; Genotype = MATa; sei1Δ::PHL, ERG6-GFP::NAT, VPH1-mCherry:HYG	This manuscript	N/A
S. cerevisiae: Name = CEN.PK; Genotype = MATa; sei1Δ::HYG	This manuscript	N/A
S. cerevisiae: Name = CEN.PK; Genotype = MATa; NVJ1-GFP::NAT; ERG6-mCherry:KanMX	This manuscript	N/A
S. cerevisiae: Name = CEN.PK; Genotype = MATa; NVJ1-GFP::NAT; VPH1-mCherry:KanMX	This manuscript	N/A
S. cerevisiae: Name = CEN.PK; Genotype = MATa; NVJ1-GFP::NAT	This manuscript	N/A
S. cerevisiae: Name = CEN.PK; Genotype = MATa; dga1Δ::HYG; lro1Δ::NAT; NVJ1-GFP::KanMX	This manuscript	N/A
S. cerevisiae: Name = CEN.PK; Genotype = MATα; dga1Δ::HYG; lro1Δ::NAT; are1Δ::NAT, are2Δ::PHL, NVJ1-GFP::KanMX	This manuscript	N/A
S. cerevisiae: Name = CEN.PK; Genotype = MATa; VPH1-mCherry:NAT	This manuscript	N/A
S. cerevisiae: Name = CEN.PK; Genotype = MATα; are1Δ::NAT, are2Δ::PHL, NVJ1-GFP::HYG	This manuscript	N/A
S. cerevisiae: Name = CEN.PK; Genotype = MATα; dga1Δ::HYG, lro1Δ::NAT, are1Δ::NAT, are2Δ::PHL, VPH1-mCherry:KanMX	This manuscript	N/A
S. cerevisiae: Name = CEN.PK; Genotype = MATa; NVJ1-GFP::NAT, SEC63-mCherry:KanMX	This manuscript	N/A
S. cerevisiae: Name = CEN.PK; Genotype = MATa; nvj1Δ::HYG; VPH1-mCherry:NAT	This manuscript	N/A
S. cerevisiae: Name = CEN.PK; Genotype = MATa; mdm1Δ::KanMX; VPH1-mCherry:NAT	This manuscript	N/A
S. cerevisiae: Name = CEN.PK; Genotype = MATa; nvj1Δ::KanMX; mdm1Δ::HGY; VPH1-mCherry:NAT	This manuscript	N/A
S. cerevisiae: Name = CEN.PK; Genotype = MATa; vac8Δ::HYG; VPH1-mCherry:NAT	This manuscript	N/A
S. cerevisiae: Name = CEN.PK; Genotype = MATa; ERG6-GFP::NAT; VPH1-mCherry:HYG	This manuscript	N/A
S. cerevisiae: Name = CEN.PK; Genotype = MATa; ldo16Δ::KanMX; ERG6-GFP::NAT; VPH1-mCherry:HYG	This manuscript	N/A
S. cerevisiae: Name = CEN.PK; Genotype = MATa; ldo45Δ::KanMX; ERG6-GFP::NAT; VPH1-mCherry:HYG	This manuscript	N/A
S. cerevisiae: Name = CEN.PK; Genotype = MATa; ldo16Δ::NAT; ldo45Δ::KanMX; ERG6-GFP::HYG; VPH1-mCherry:PHL	This manuscript	N/A
S. cerevisiae: Name = CEN.PK; Genotype = MATa; LDO16/45-GFP::NAT; VAC8-mCherry:KanMX	This manuscript	N/A

(*Continued on next page*)

Continued

REAGENT or RESOURCE	SOURCE	IDENTIFIER
S. cerevisiae: Name = CEN.PK; Genotype = MATa; VAC8-mCherry:KanMX	This manuscript	N/A
S. cerevisiae: Name = CEN.PK; Genotype = MATa; nvj1Δ::HYG; VAC8-mCherry:KanMX	This manuscript	N/A
S. cerevisiae: Name = CEN.PK; Genotype = MATa; ldo16Δ::NAT; ldo45Δ::HYG; VAC8-mCherry:KanMX	This manuscript	N/A
S. cerevisiae: Name = CEN.PK; Genotype = MATa; nvj1Δ::PHL; ldo16Δ::KanMX; ldo45Δ::HYG; VPH1-mCherry:NAT	This manuscript	N/A
S. cerevisiae: Name = CEN.PK; Genotype = MATa; ldo16Δ::KanMX; ldo45Δ::HGY; NVJ1-GFP::NAT	This manuscript	N/A
S. cerevisiae: Name = CEN.PK; Genotype = MATa; HO-GAP-LDO16:KanMX; NVJ1-GFP::NAT	This manuscript	N/A
S. cerevisiae: Name = CEN.PK; Genotype = MATa; ldo16Δ::KanMX, ldo45Δ::HYG, VPH1-mCherry:NAT	This manuscript	N/A
S. cerevisiae: Name = CEN.PK; Genotype = MATa; vac8Δ::KanMX	This manuscript	N/A
S. cerevisiae: Name = CEN.PK; Genotype = MATa; nvj1Δ::HGY	This manuscript	N/A
S. cerevisiae: Name = CEN.PK; Genotype = MATa; nvj1Δ::HYG; mdm1Δ::NAT	This manuscript	N/A
S. cerevisiae: Name = CEN.PK; Genotype = MATa; ldo16Δ::NAT; ldo45Δ::KanMX	This manuscript	N/A
S. cerevisiae: Name = CEN.PK; Genotype = MATa; nvj1Δ::PHL; ldo16Δ::KanMX; ldo45Δ::HYG	This manuscript	N/A
S. cerevisiae: Name = CEN.PK; Genotype = MATa; OSH1-GFP::NAT	This manuscript	N/A
S. cerevisiae: Name = CEN.PK; Genotype = MATa; HO-GAP-MDM1-GFP::HYG	This manuscript	N/A
S. cerevisiae: Name = CEN.PK; Genotype = MATa; VAC8-GFP::KanMX	This manuscript	N/A
S. cerevisiae: Name = CEN.PK; Genotype = MATa; snd3Δ::HYG, NVJ1-GFP::NAT, VPH1-mCherry:KanMX	This manuscript	N/A
S. cerevisiae: Name = CEN.PK; Genotype = MATa; snd3Δ::HYG, NIC96-GFP::NAT, VPH1-mCherry:KanMX	This manuscript	N/A
S. cerevisiae: Name = CEN.PK; Genotype = MATa; ERG6-GFP::NAT; LDO16/45-mCherry:KanMX	This manuscript	N/A
S. cerevisiae: Name = CEN.PK; Genotype = MATa; ldo16Δ::KanMX, VPH1-mCherry:NAT	This manuscript	N/A
S. cerevisiae: Name = CEN.PK; Genotype = MATa; ldo45Δ::KanMX, VPH1-mCherry:NAT	This manuscript	N/A
S. cerevisiae: Name = CEN.PK; Genotype = MATa; ldo16Δ::NAT; ldo45Δ::KanMX; ERG6-GFP::HYG	This manuscript	N/A
S. cerevisiae: Name = CEN.PK; Genotype = MATa; nvj1Δ::NAT; mdm1Δ::HYG; ERG6-GFP::KanMX	This manuscript	N/A
S. cerevisiae: Name = CEN.PK; Genotype = MATa; HO-GAP-PCT1:HYG	This manuscript	N/A
S. cerevisiae: Name = CEN.PK; Genotype = MATa; nvj1Δ::NAT, HO-GAP-MDM1:HYG	This manuscript	N/A
S. cerevisiae: Name = CEN.PK; Genotype = MATa; nvj1Δ::HYG, mdm1Δ::NAT, HO-GAP-LDO16:KanMX	This manuscript	N/A
S. cerevisiae: Name = CEN.PK; Genotype = MATa; ldo16Δ::NAT, ldo45Δ::KanMX, HO-GAP-NVJ1:HYG	This manuscript	N/A

(*Continued on next page*)

Continued

REAGENT or RESOURCE	SOURCE	IDENTIFIER
Software and Algorithms		
IMOD	Kremer et al.[48]	https://bio3d.colorado.edu/imod/
AMIRA 6.8	Thermo Fisher Scientific	N/A
OLYMPUS CellSens Dimension	Olympus Corporation	https://www.olympus-lifescience.com.cn/
Imaris 10.0.0	Bitplane AG	https://imaris.oxinst.com/
softWoRx	Applied Precision, GE	https://softworx.com/
ImageJ	N/A	https://imagej.net/ij/

EXPERIMENTAL MODEL AND SUBJECT DETAILS

All yeast strains used in this study are listed in the key resources table. All strains and genetic manipulations were verified by sequencing and phenotype. The prototrophic CEN.PK strain background was used in all experiments. Gene deletions and C-terminal tag were carried out using standard PCR-based strategies to amplify resistance cassettes with appropriate flanking sequences and replacing or inserting the target fragment by homologous recombination.[49] Strains with overexpression of a certain gene were constructed by targeted integration of genes of interest driven by the glyceraldehydes-3-phosphate dehydrogenase (GAP) promoter at the HO chromosomal locus.

Media used in this study: rich medium (YP) containing 2% yeast extract, 2% peptone, and 2% different carbon sources, including lactate (L), glucose (D), glycerol (G), or ethanol (E), and synthetic defined minimal medium (S) containing 0.17% yeast nitrogen base without amino acids containing 0.5% ammonium sulfate (Difco) with 2% different carbon sources including lactate, glucose, glycerol, or ethanol. The percentages provided here are expressed as weight/volume (w/v). For nutrient deprivation, cells were inoculated in YPL rich medium overnight, then diluted with fresh YPL medium, grown to the logarithmical phase, and switched to SL minimal medium. In our study, we used sodium lactate (pH 6.3) rather than lactic acid in the lactate-containing growth media. The pH of YPL medium is 5.7, while that of SL medium is 5.1. For comparison, the pH of YPD, YPE, and YPG media is approximately 6.5, whereas the pH of SD, SE, and SG media is around 4.4. After culturing cells to log phase and prior to the nutrient deprivation switch, the pH of YPD, YPE, YPG, and YPL media was measured at 6.2, 6.3, 6.7, and 6.0, respectively. The pH values for cells growing in YPL prior to nutrient deprivation were not drastically different compared to other carbon sources. However, the nutrient deprivation medium containing lactate was slightly more alkaline than those with other carbon sources. Therefore, it is unlikely that our observations were influenced by acidic pH stress caused by lactate.

METHOD DETAILS

Transmission electronic microscopy (TEM) imaging

Yeast cells were collected and fixed with a three-step protocol.[50,51] Cells were first fixed in a solution of 1.5% (w/v) $KMnO_4$ for 20 min at room temperature. After centrifugation and rinsing with 100 mM phosphate buffer (pH 7.0) for three times, the cells were next fixed in 2.5% glutaraldehyde at 4°C overnight. After centrifugation and wash, the cells were again fixed in 1% osmium tetroxide for 2 h at room temperature avoiding illumination. The fixed yeast samples were dehydrated using ethanol and acetone of gradient concentrations. Next, the samples were embedded into Epon 812 resin (SPI supplies Inc. PA, USA) and heated for polymerization under 60°C to preserve fine structure in solid blocks. Ultra-thin sections (70 nm) of the samples were resolved using a Leica UC 6 microtome (Leica, Vienna, Austria) with a diamond knife (Diatome, Switzerland) and placed onto 200 mesh copper grids. The sample sections were put into an H-7650 TEM (Hitachi, Ibaraki, Japan) for observation at 80 kV of accelerating voltage. The images were acquired with a Gatan 830 CCD camera (Gatan, CA, USA).

Electron tomography (ET) and 3D reconstruction

200 nm sections cut from the Epon resin blocks for ET reconstruction were placed onto 100 mesh carbon-covered copper grids and applied by 10 nm colloidal gold particles (Sigma, St. Louis, MO). Data were collected automatically from a JEOL 2010 TEM (JEOL, Tokyo, Japan) at 200 kV. Computation and reconstruction of the electron tomographs were done by the IMOD 'etomo' program according to the software manual.[48] The 3D structure was processed using the software Amira 6.8 (Thermo Fisher Scientific), including stack making, alignment, and color assigning.

3D imaging of a subcellular bearing using FIB-SEM

Yeast cells were first collected and fixed for FIB-SEM imaging. The cells were fixed in 1.5% (w/v) $KMnO_4$ for 20 min at room temperature. After centrifugation and wash steps, the cells were then re-suspended in 2.5% glutaraldehyde at 4°C overnight. After 1 h of treatment with 1% osmium tetroxide/1.5% potassium ferrocyanide (w/v) on ice, the samples were washed, sequentially treated

with 1% thiocarbohydrazide at room temperature for 20 min, 2% aqueous osmium tetroxide at room temperature for 30 min, 1% aqueous uranyl acetate at 4°C overnight, and 0.66% lead nitrate in 30 mM L-aspartic acid at 60°C for 30 min. Next, the samples were dehydrated using a series of gradient ethanol and then embedded into Epon 812 resin at 60°C for 48 h.

For imaging, resin blocks with the yeast cell samples were carefully trimmed with a trimmer (EM TXP, Leica) to expose the surface containing yeast cells at the top of the resin block. The trimmed blocks were then mounted on a 90° stub and coated with platinum by an ion sputtering apparatus (EM ACE200, Leica) for 300 s. We next identified an area of a subcellular bearing as a target by scanning electron microscopy (Teneo VS, Thermo). Next, the area surrounding the target was trenched and smoothed out by an ultra-microtome in the specimen chamber. The resin block was then transferred to a 45° tilted stub and coated with platinum by ion sputtering apparatus. SEM Imaging was performed using a dual beam SEM (FIB Helious G3 UC; Thermo Fisher). The data were acquired in the serial surface view mode with a slice thickness of 10 nm at 30 kV and 0.79 nA. Each surface was serially imaged at 2 kV acceleration voltage and 0.2 nA current in backscatter electron mode with an in-column backscatter electron detector. The images were then aligned, filtered, and manually segmented to generate surfaces for 3D presentation in Amira 6.8.

3D reconstruction using spinning disk confocal microscopy and Imaris

z stack images were acquired using a spinning disk confocal microscope model (Olympus) equipped with a 100×, 1.4 NA oil objective lens. Sequential optical sections were collected at 0.2 μm intervals across a total depth of 6 μm. Samples were excited with 405nm, 488 nm, 561 nm to visualize the nucleus (Nup60-NLS-CFP), LDs (BODIPY) and the vacuole (Vph1-mCherry). All images were deconvolved using the software OLYMPUS cellSens Dimension.

For 3D reconstruction, z stack images from three channels were imported into Imaris software (Bitplane AG, version 10.0.0). Surface rendering and volume reconstruction were performed using the Surpass mode with "Spot" (LDs) and "Surface" (the nucleus and vacuole). Channels were pseudo-colored to represent nucleus in blue, LDs in green, vacuole in red. Final 3D models were exported as TIFF and AVI for visualization.

Live cell imaging

Yeast cells were cultured in YPL rich medium in the logarithmic phase and switched to SL minimal medium for nutrient deprivation. The cells at indicated phases were used for live cell imaging with corresponding cell organelles illuminated by the indicated GFP and mCherry proteins. The GFP and mCherry tags were chromosomally integrated at the C terminus of the genes of interest. Images were taken by Deltavision Elite microscope (Applied Precision, GE) under a 100×, 1.4 NA oil-immersion objective lens. All images were deconvolved using the software softWoRx.

For time-resolved live cell imaging, the cells starved for 4h in SL minimal medium were immobilized on concanavalin-A-coated coverslips.[52] To examine the process of bearing formation, images were taken every 3 min for 2.5 h at 30°C using a SpinSR microscope (Olympus) equipped with a SoRa disk (Olympus Super Resolution, OSR) under a 100×, 1.4 NA oil objective lens. All images were deconvolved using the software OLYMPUS cellSens Dimension.

BODIPY 493/503 staining of LDs

BODIPY 493/503 (Thermo Fisher) was added to yeast cells in liquid growth medium at a final concentration of 5.7 μM. After incubation in a shaker (280 rpm, 30°C) for 20 min, LD staining was observed under a fluorescence microscope.

AUTODOT staining of LDs

Yeast cells in liquid growth medium were treated with AUTODOT (Abcepta) at 100 μM final concentration. After 20 min of incubation with constant shaking (280 rpm, 30°C), LDs were visualized by fluorescence microscopy.

Lipid extraction and quantification by mass spectrometry

Yeast cell lipids were extracted with chloroform/methanol (2:1) (v/v) as described previously.[31,53] In brief, 10 OD_{600} units of cells were used for lipid extraction. The samples were resuspended in 500 μL mass spectrometry-grade methanol containing 17:0 PC, 17:0 PE, and 14:0 PS as spike-in standards and lysed by bead-beating. The lysates were then transferred to glass tubes, added another 500 μL methanol, 2 mL chloroform, and vortex for lipid extraction. After centrifugation, the supernatants were transferred to glass tubes. Additional 800 μL chloroform and 400 μL of 50 mM citric acid were added to achieve phase separation. The lipid phase was equally taken and were dried by a vacuum concentrator system (Labconco).

A triple quadrupole mass spectrometer (the QTRAP 6500 + System) was used for lipid quantitative analysis according to an established protocol.[53] For phospholipid quantification, a mix of MS-grade isopropanol, acetonitrile, water (2:1:1) containing Lipidomix (Avanti) was used to dissolve lipid extracts. For the quantification of neutral lipids such as TAG and sterol ester, a mixture of methanol and dichloromethane (1:1, v/v) containing 5 mM ammonium acetate and Lipidomix was used to dissolve lipid extracts. Lipids separated chromatographically on a C18 column (ACQUITY UPLC BEH C18 column, 130A, 1.7 μm, 2.1 mm × 50 mm) were followed by quantification using multiple reaction monitoring (MRM) transitions of mass spectrometry. Specifically, liquid chromatography was programmed below: Buffer A contains 33.3% methanol, 33.3% acetonitrile, 33.4% water, 5 mM ammonium acetate, and Buffer B contains 5 mM ammonium acetate in 100% isopropanol. The retention time for each MRM peak was compared to an appropriate standard. The area under each peak was quantitated using Analyst software, re-inspected for accuracy.

Determination of survival rates

Survival rates were determined using both the single colony formation assay and the spotting assay as previously described.[31] Nutrient deprivation was performed by switching yeast cells growing exponentially in YPL rich medium to SL minimal medium. To measure survival rates, after indicated hours, an aliquot of liquid culture was taken, diluted, and spread on YP glucose plates for colony formation or for spotting. For the single colony formation assay, the rate of survival was calculated by the following formula: Survival rate% = 100* the number of colonies at an indicated nutrient deprivation time point * dilution factor/(number of colonies at 12 h nutrient deprivation * dilution factor). Of note, cells proliferated very slowly under nutrient deprivation. After 12 h of nutrient deprivation, the optical density (OD) at 600 nm and the number of colonies formed per OD units were similar between WT and the mutant strains, which ensures an appropriate normalization point for calculating survival rates. The spotting assay involves serial 10-fold dilutions of cells that were starved for the indicated time periods and then spotted onto rich-medium plates. Unlike the single colony formation assay, the growth difference in the spotting assay can reveal survival differences while having lower resolution.

Whole yeast cell extracts preparation and western blotting

A urea-based protocol was used to lyse yeast cells for western blots. Cells were spun down, quenched in 20% trichloroacetic acid on ice for 15 min, washed with acetone. Cell pellets were resuspended in urea buffer containing 50 mM Tris-Cl pH 7.5, 5 mM EDTA, 6 M urea, 1% SDS, 1 mM PMSF, 2 mM sodium orthovanadate, and 50 mM NaF, and lysed by bead-beating. After collecting the supernatants, protein concentration was determined using Pierce BCA protein assay. The same amount of proteins was separated using SDS-PAGE gels, transferred to a nitrocellulose membrane or a PVDF membrane, and blotted with the corresponding antibodies. Blocking was performed in 5% dry milk/TBST, and antibody incubation was in 1% dry milk/TBST. Antibodies used in this study is mouse anti-GFP antibody (Roche, Cat. No. 11814460001, 1:5000), which is commercially available and validated. Uncropped and unprocessed scans of the blots are provided in the Source Data file. ImageJ (v1.8.0, National Institutes of Health) was used for Western blot densitometry analysis.

QUANTIFICATION AND STATISTICAL ANALYSIS

NVJ length

ImageJ software was utilized to assess the length of the NVJ. Prior to measurement, the scale was calibrated based on the scale bars in the fluorescence microscope images. The NVJ length was determined using the freehand line tool in ImageJ. To ensure statistical robustness, the NVJ length was quantified in a minimum of 95 cells for each independent experiment.

LD size

ImageJ software was utilized to assess the size of LDs. Prior to measurement, the scale was calibrated based on the scale bars in the fluorescence microscope images. LD sizes were determined using the straight line tool in ImageJ. To ensure statistical robustness, LD sizes were quantified in a minimum of 100 cells for each independent experiment.

Quantification of the percentage of the subcellular bearing

Given the dynamic nature of a subcellular bearing, we distinguished two types of bearing structures: standard bearings and partial bearings. A subcellular bearing is categorized as standard if the nucleus was fully enveloped, and as partial if more than half of the nucleus was enveloped by the vacuole. The cell counter tool in ImageJ was used to mark out the cells with the bearing. Both types of bearing structures were considered as subcellular bearings and were quantified in at least three independent experiments with a minimum of 200 cells counted.

Statistical analysis

ImageJ was used to determine the number and size of LDs and the length of NVJ. Statistical data were presented as the mean ± standard deviation (SD) from at least two biological independent experiments. The representatives of n are specified in figure legends. The statistical significance in related figures was tested using two-tailed Student's *t* test or one-way ANOVA. Figure 1F, 1G, 2B, 4D, 4F, 4H, 4J, 5D, 6B, 6E, 7B, 7C, and S2D were tested using one-way ANOVA and other figures were tested using two-tailed Student's *t* test. Differences were considered statistically significant when p values were less than 0.05. *, $p < 0.05$; **, $p < 0.01$; ***, $p < 0.001$.

Cell Reports, Volume *44*

Supplemental information

An adaptive organelle triad houses lipid droplets for dynamic regulation

Hong Qiu, Can Miao, and Cunqi Ye

Figure S1

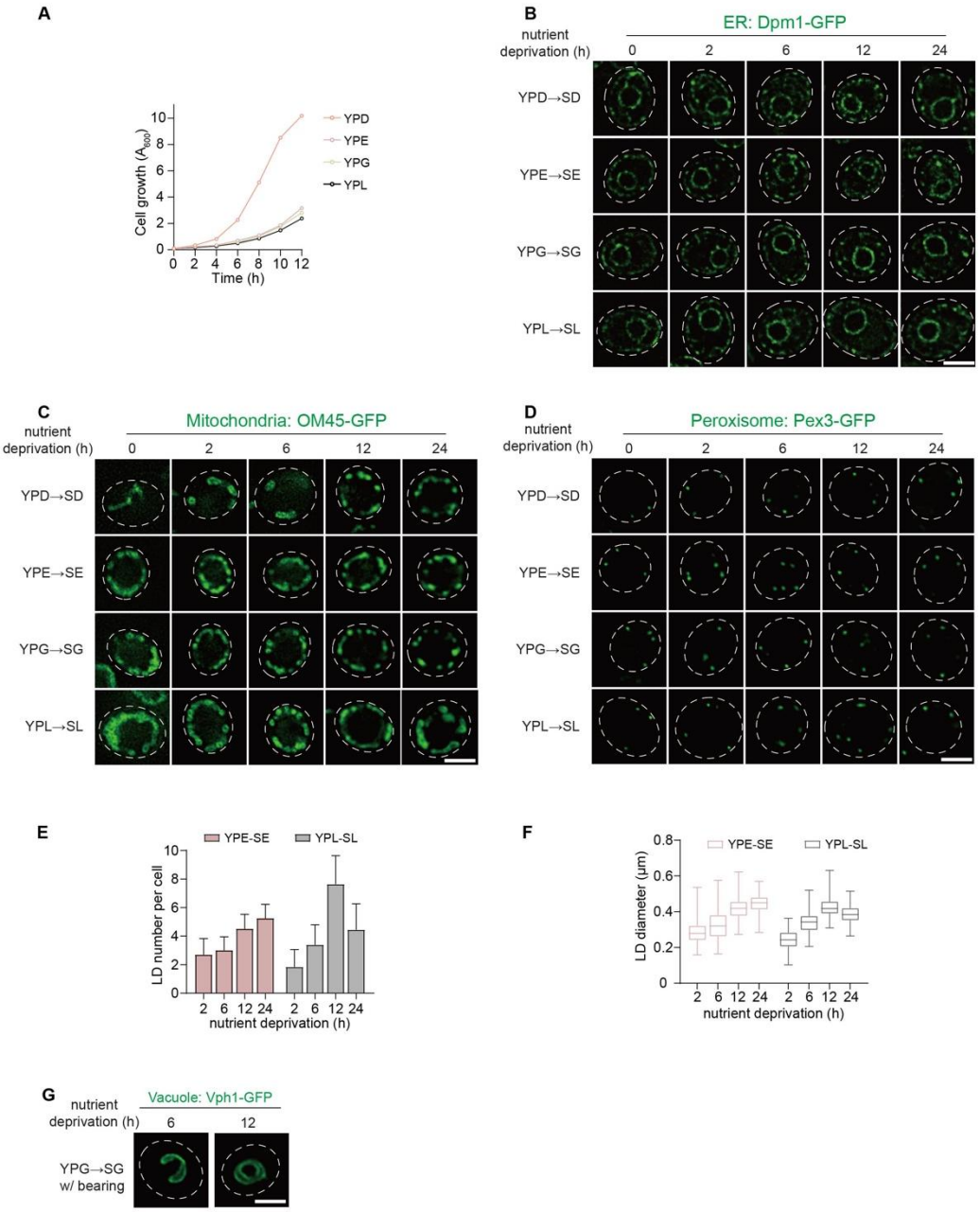
A
Cell growth (A_{600})
Time (h)
YPD
YPE
YPG
YPL
B
ER: Dpm1-GFP
nutrient deprivation (h)
0 2 6 12 24
YPD→SD
YPE→SE
YPG→SG
YPL→SL
C
Mitochondria: OM45-GFP
D
Peroxisome: Pex3-GFP
E
YPE-SE
YPL-SL
LD number per cell
nutrient deprivation (h)
F
LD diameter (μm)
G
Vacuole: Vph1-GFP
YPG→SG w/ bearing

Figure S1. Morphological screening of major organelle responses to nutrient deprivation under varying carbon sources, related to Figure 1.

(A) Growth curves of WT cells cultured in rich medium with different carbon sources. Data are represented as mean ± SD (n=4 biologically independent samples).

(B-D) Live-cell imaging of the ER labeled with Dpm1-GFP (B), mitochondria labeled with OM45-GFP (C), and peroxisomes with Pex3-GFP (D) in WT cells in rich medium and after 2, 6, 12, and 24 hours of nutrient deprivation with different carbon sources. Scale bar, 2 μm.

(E) Quantification of LD numbers in WT cells after 2, 6, 12, and 24 hours of nutrient deprivation from live-cell imaging. Data shown are representative of experiments repeated twice and are represented as mean ± SD (n=200 for ethanol nutrient deprivation and 256 for lactate nutrient deprivation at each time point; n=number of cells).

(F) Quantification of LD diameters in WT cells after 2, 6, 12, and 24 hours of nutrient deprivation from live-cell imaging. Data shown are representative of experiments repeated twice and are represented as mean ± SD (n=215, 256, 256, 244 for ethanol nutrient deprivation and 208, 204, 216, 203 for lactate nutrient deprivation at corresponding time points; n=number of LDs).

(G) Representative images illustrating vacuolar deformation in glycerol-containing minimal medium after 6 and 12 hours of nutrient deprivation.

Figure S2

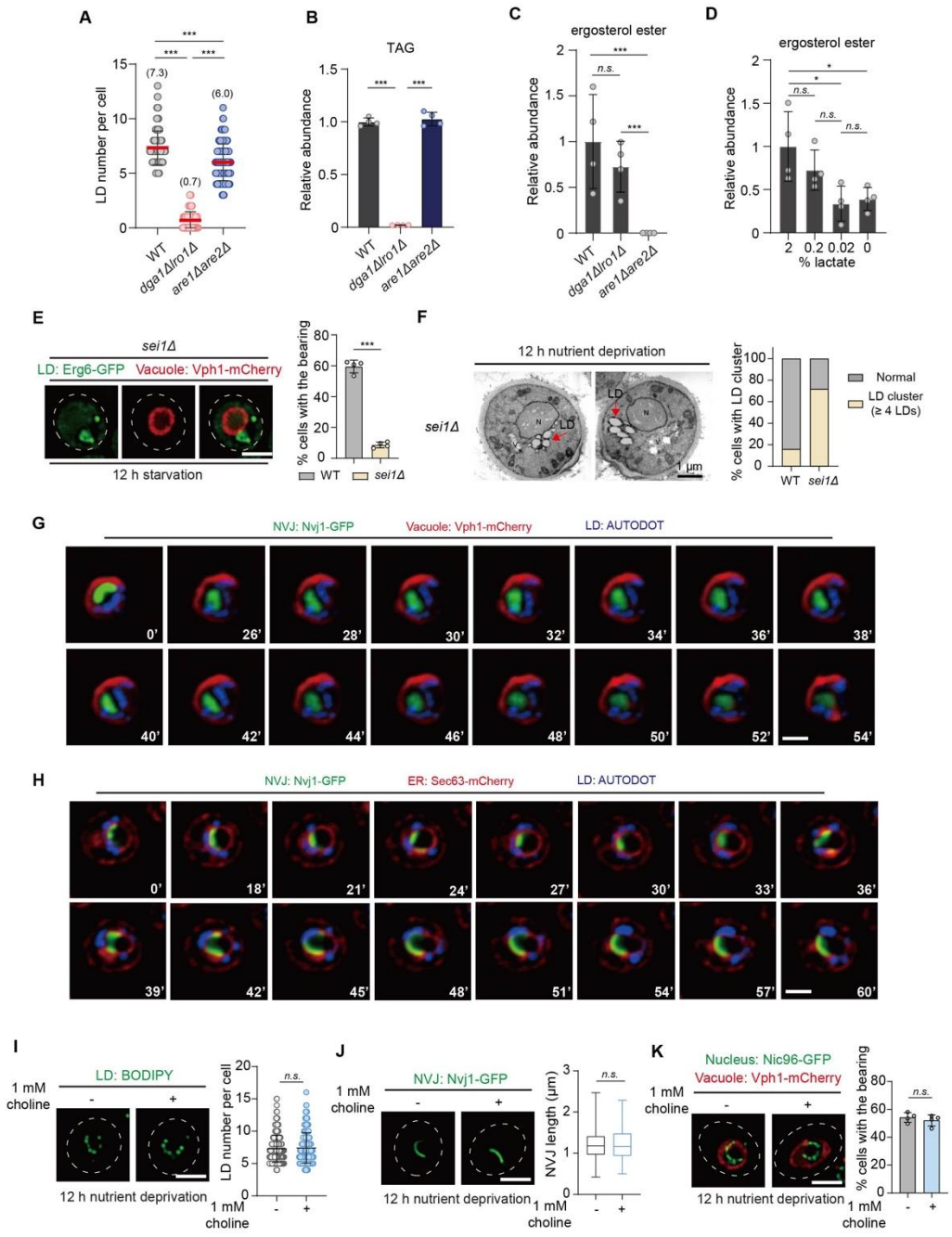
A
LD number per cell
(7.3)
(0.7)
(6.0)
WT
dga1Δlro1Δ
are1Δare2Δ
B
TAG
Relative abundance
C
ergosterol ester
Relative abundance
D
ergosterol ester
Relative abundance
% lactate
E
sei1Δ
LD: Erg6-GFP Vacuole: Vph1-mCherry
12 h starvation
% cells with the bearing
WT sei1Δ
F
12 h nutrient deprivation
sei1Δ
LD
1 μm
% cells with LD cluster
Normal
LD cluster (≥ 4 LDs)
G
NVJ: Nvj1-GFP Vacuole: Vph1-mCherry LD: AUTODOT
H
NVJ: Nvj1-GFP ER: Sec63-mCherry LD: AUTODOT
I
LD: BODIPY
1 mM choline
12 h nutrient deprivation
LD number per cell
J
NVJ: Nvj1-GFP
NVJ length (μm)
K
Nucleus: Nic96-GFP
Vacuole: Vph1-mCherry
% cells with the bearing
n.s.

Figure S2. LD biogenesis is required for subcellular bearing formation and survival under nutrient deprivation, related to Figure 4.

(A) Quantification of LD number after 12 hours of nutrient deprivation in WT, *dga1Δlro1Δ*, and *are1Δare2Δ* cells. Data are represented as mean ± SD (n=279 for WT, n=200 for *dga1Δlro1Δ,* n=140 *are1Δare2Δ*; n=number of cells). ***, $p<0.001$.

(B-C) TAG (B) and sterol ester (C) levels determined using mass spectrometry in WT, *dga1Δlro1Δ*, and *are1Δare2Δ* cells starved for 12 h. Data are represented as mean ± SD (n=4 biologically independent samples). ***, $p<0.001$.

(D) Sterol ester levels in WT cells undergoing 12 hours of nutrient deprivation in the presence of varying concentrations of lactate. Data are represented as mean ± SD (n=4 biologically independent samples). *, $p<0.05$; *n.s.*, no significance.

(E) Left: Live-cell imaging of cells with Erg6-GFP and Vph1-mCherry in *sei1Δ* cells. Right: Quantification of subcellular bearing formation in WT and *sei1Δ* cells after 12 hours of nutrient deprivation. Data are represented as mean ± SD (n=4 independent experiments; more than 200 cells were quantified). ***, $p<0.001$.

(F) Left: TEM images of *sei1Δ* cells after 12 hours of nutrient deprivation. Scale bar, 1 μm. N, nucleus; V, vacuole; LD, lipid droplet. Right: Quantification of cells with clustered LDs in WT and *sei1Δ* cells after 12 hours of nutrient deprivation from TEM data. 100 cells were quantified per genotype.

(G-H) Time-lapse confocal spinning-disk microscopy of nuclear ER, NJV, vacuole, and LD dynamics under nutrient deprivation in WT cells, using three fluorophores. (G) NVJ (Nvj1-GFP), Vacuole (Vph1-mCherry), LD (AUTODOT). (H) NVJ (Nvj1-GFP), ER (Sec63-mCherry), LD (AUTODOT). Scale bar, 2 μm.

(I) BODIPY staining of LDs and quantification in WT cells ± 1 mM choline after 12 hours of nutrient deprivation. Data are mean ± SD (n=277/221 cells).

(J) Nvj1-GFP imaging of NVJ and quantification in WT cells ± 1 mM choline after 12 hours of nutrient deprivation. Data are mean ± SD (n=212/213 cells).

(K) Nic96-GFP/Vph1-mCherry imaging and quantification of bearing formation in WT cells ± 1 mM choline after 12 hours of nutrient deprivation. Data are mean ± SD (n=4 experiments, >200 cells/experiment). *n.s.*, no significance.

Figure S3

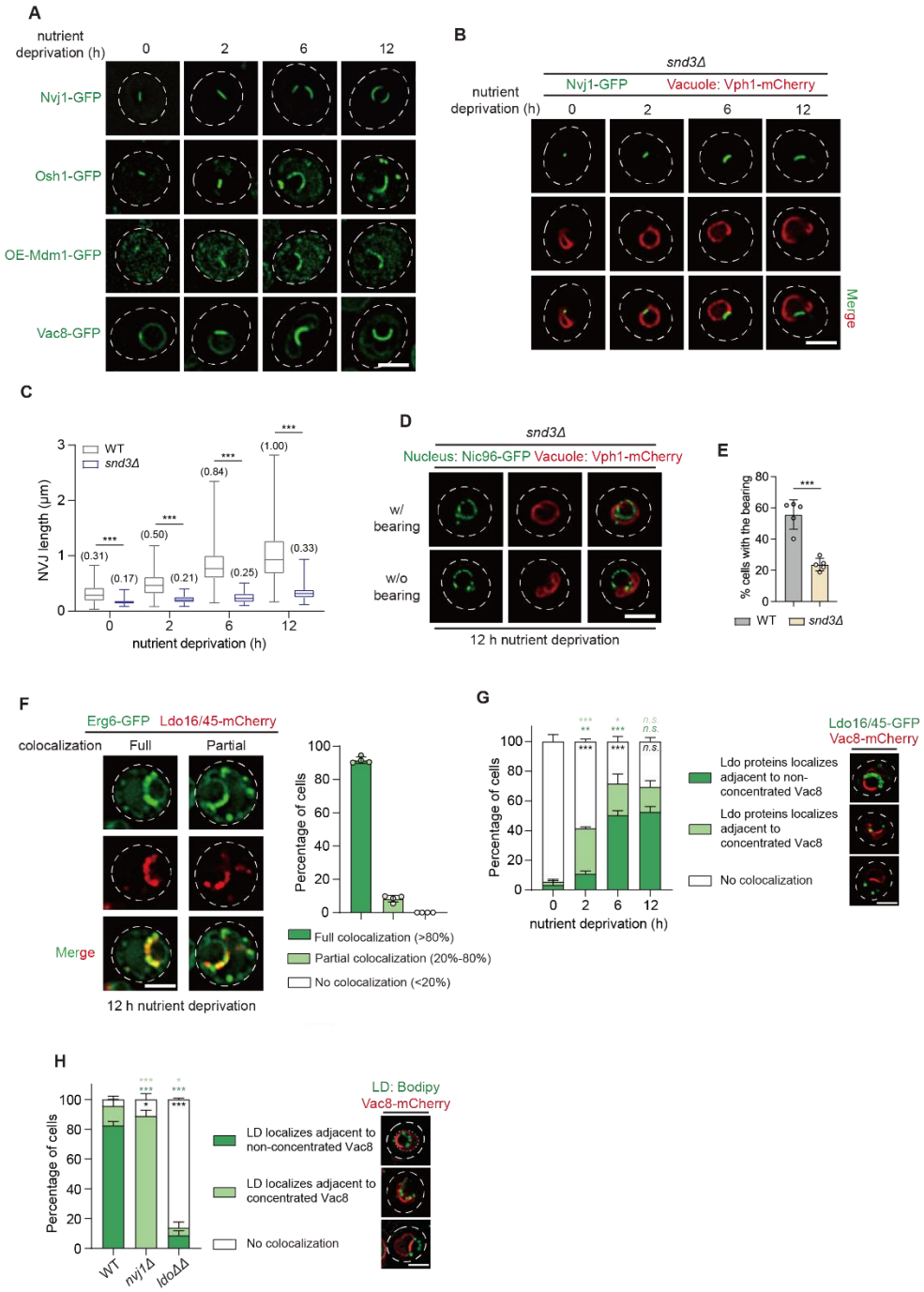
A
nutrient deprivation (h)
0
2
6
12
Nvj1-GFP
Osh1-GFP
OE-Mdm1-GFP
Vac8-GFP
B
snd3Δ
Nvj1-GFP
Vacuole: Vph1-mCherry
nutrient deprivation (h)
0
2
6
12
Merge
C
WT
snd3Δ
NVJ length (μm)
(0.31)
(0.17)
(0.50)
(0.21)
(0.84)
(0.25)
(1.00)
(0.33)
***
nutrient deprivation (h)
D
snd3Δ
Nucleus: Nic96-GFP Vacuole: Vph1-mCherry
w/ bearing
w/o bearing
12 h nutrient deprivation
E
% cells with the bearing
***
WT
snd3Δ
F
Erg6-GFP Ldo16/45-mCherry
colocalization
Full
Partial
Merge
12 h nutrient deprivation
Percentage of cells
Full colocalization (>80%)
Partial colocalization (20%-80%)
No colocalization (<20%)
G
Percentage of cells
nutrient deprivation (h)
Ldo proteins localizes adjacent to non-concentrated Vac8
Ldo proteins localizes adjacent to concentrated Vac8
No colocalization
Ldo16/45-GFP
Vac8-mCherry
H
Percentage of cells
WT
nvj1Δ
ldoΔΔ
LD localizes adjacent to non-concentrated Vac8
LD localizes adjacent to concentrated Vac8
No colocalization
LD: Bodipy
Vac8-mCherry

Figure S3. Vac8-mediated vCLIP and NVJ contacts are critical for the formation of subcellular bearing structures, related to Figure 6.

(A) Live-cell imaging of cells with Nvj1-GFP, Osh1-GFP, *MDM1* overexpression (*OE*-Mdm1-GFP), and Vac8-GFP under rich medium and after 2, 6, 12 hours of nutrient deprivation. Scale bar, 2 μm.

(B) Live-cell imaging of *snd3Δ* cells with Nvj1-GFP and Vph1-mCherry under rich medium and after 2, 6, 12 hours of nutrient deprivation. Scale bar, 2 μm.

(C) Quantification of NVJ length during nutrient deprivation in WT and *snd3Δ* cells using Nvj1-GFP. Data shown are representative of experiments repeated twice and represented as mean ± SD (n=133, 152, 195, 615 for WT, n=98, 246, 232, 220 for *sndΔ*; n=number of cells). ***, $p<0.001$.

(D) Live-cell imaging of *snd3Δ* cells with Nic96-GFP and Vph1-mCherry under 12 hours of nutrient deprivation. Scale bar, 2 μm.

(E) Quantification of subcellular bearing formation in WT and *snd3Δ* cells after 12 hours of nutrient deprivation. Data are represented as mean ± SD (n=5 independent experiments; more than 200 cells were quantified). ***, $p<0.001$.

(F) Left: Live-cell imaging of LDs labeled with Erg6-GFP and Ldo16/45-mCherry in WT cells after 12 hours of nutrient deprivation. Right: Quantification of the percentage of full, partial, and no colocalization between LDs and Ldo16/45 in WT cells. Data are represented as mean ± SD (n=4 independent experiments).

(G) Quantification of LDO-Vac8 spatial localization in WT cells under nutrient deprivation. Data are mean ± SD (n=3 experiments, >200 cells/experiment). *, $p<0.05$; **, $p<0.01$; ***, $p<0.001$; *n.s.*, no significance. Asterisks denote comparisons between nutrient-rich and deprivation conditions; black asterisks for no colocalization, green for column-matched groups.

(H) Quantification of LD-Vac8 spatial localization in WT, *nvj1Δ*, and *ldo16Δldo45Δ* cells. Data are mean ± SD (n=3 experiments, >200 cells/experiment). *, $p<0.05$; ***, $p<0.001$. Asterisks denote comparisons between WT and mutants; black asterisks for no colocalization, green for column-matched groups.

Figure S4

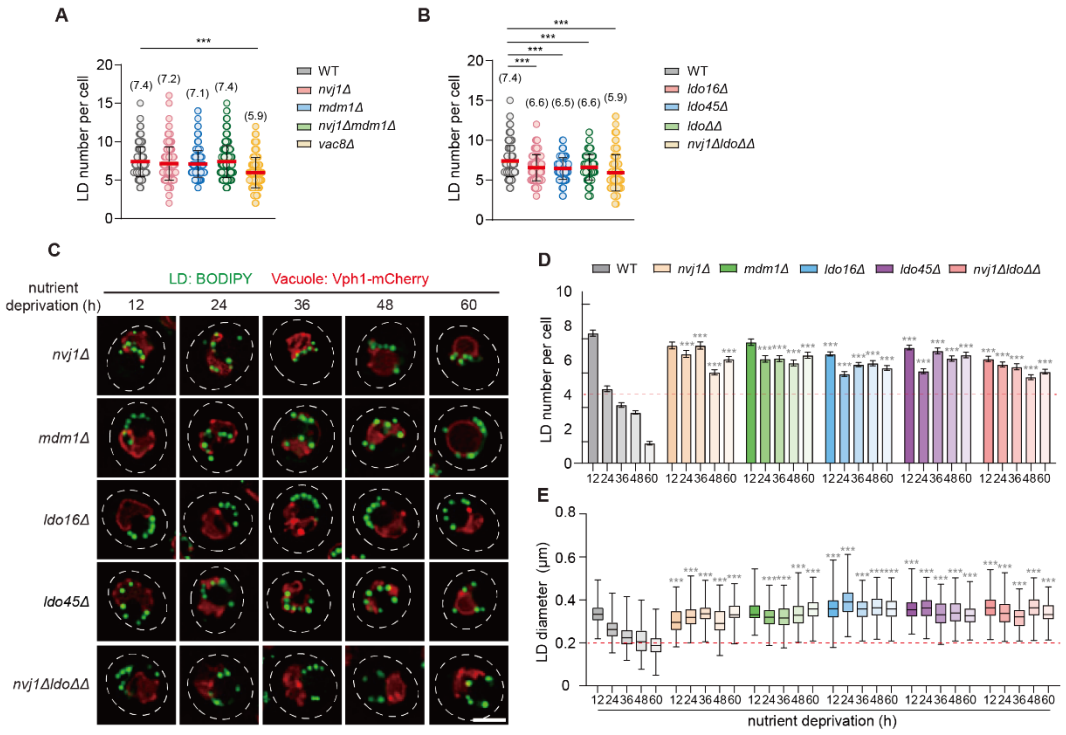
A
B
LD number per cell
WT
nvj1Δ
mdm1Δ
nvj1Δmdm1Δ
vac8Δ
ldo16Δ
ldo45Δ
ldoΔΔ
nvj1ΔldoΔΔ
C
nutrient deprivation (h)
LD: BODIPY
Vacuole: Vph1-mCherry
D
E
LD diameter (μm)
nutrient deprivation (h)

Figure S4. Subcellular bearings facilitate efficient LD turnover and adaptation to nutrient stress, related to Figure 7.

(A) Quantification of LD numbers after 12 hours of nutrient deprivation in WT, *nvj1Δ*, *mdm1Δ*, *nvj1Δmdm1Δ*, and *vac8Δ* cells. Data shown are representative of experiments repeated twice and represented as mean ± SD (n=321 for WT, 195 for *nvj1Δ*, 285 for *mdm1Δ*, 315 for *nvj1Δmdm1Δ*, and 403 for *vac8Δ*; n=number of cells).

(B) Quantification of LD numbers after 12 hours of nutrient deprivation in WT, *ldo16Δ*, *ldo45Δ*, *ldo16Δldo45Δ*, and *nvj1Δldo16Δldo45Δ* cells. Data shown are representative of experiments repeated twice and represented as mean ± SD (n=321 for WT, 174 for *ldo16Δ*, 151 for *ldo45Δ*, 159 for *ldo16Δldo45Δ*, 145 for *nvj1Δldo16Δldo45Δ*; n=number of cells).

(C) Live-cell imaging of LDs stained with BODIPY and the vacuole labeled with Vph1-mCherry in *nvj1Δ*, *mdm1Δ*, *ldo16Δ, ldo45Δ*, and *nvj1Δldo16Δldo45Δ* cells after 12, 24, 36, 48, and 60 hours of nutrient deprivation. Scale bar, 2 μm.

(D) Quantification of LD numbers in WT, *nvj1Δ*, *mdm1Δ*, *ldo16Δ, ldo45Δ*, and *nvj1Δldo16Δldo45Δ* cells after 12, 24, 36, 48, and 60 hours of nutrient deprivation. Data shown are representative of experiments repeated twice and are represented as mean ± SD (n=138, 174, 154, 256, 242 for WT; n=184, 193, 178, 209, 210 for *nvj1Δ*; n=201, 195, 201, 205, 196 for *mdm1Δ*; n=171, 213, 209, 209, 209 for *ldo16Δ*; n=203, 213, 200, 210, 214 for *ldo45Δ*; n=220, 204, 208, 212, 208 for *nvj1Δldo16Δldo45Δ*; n=number of cells). ***, $p<0.001$. Grey asterisks indicate statistical significance for comparisons between WT and the mutant cells at the same time point.

(E) Quantification of LD diameters in *nvj1Δ*, *mdm1Δ*, *ldo16Δ, ldo45Δ*, and *nvj1Δldo16Δldo45Δ* cells after 12, 24, 36, 48, and 60 hours of nutrient deprivation. Data are represented as mean ± SD (n= 238, 256, 212, 238, 231 for WT; n=259, 208, 217, 216, 204 for *nvj1Δ*; n=241, 221, 214, 313, 214 for *mdm1Δ*; n=274, 261, 213, 226, 229 for *ldo16Δ*; n=267, 221, 268, 233, 249 for *ldo45Δ*; n=210, 212, 207, 214, 223 for *nvj1Δldo16Δldo45Δ*; n=number of cells). ***, $p<0.001$. Grey asterisks indicate statistical significance for comparisons between WT and the mutant cells at the same time point.

Figure S5

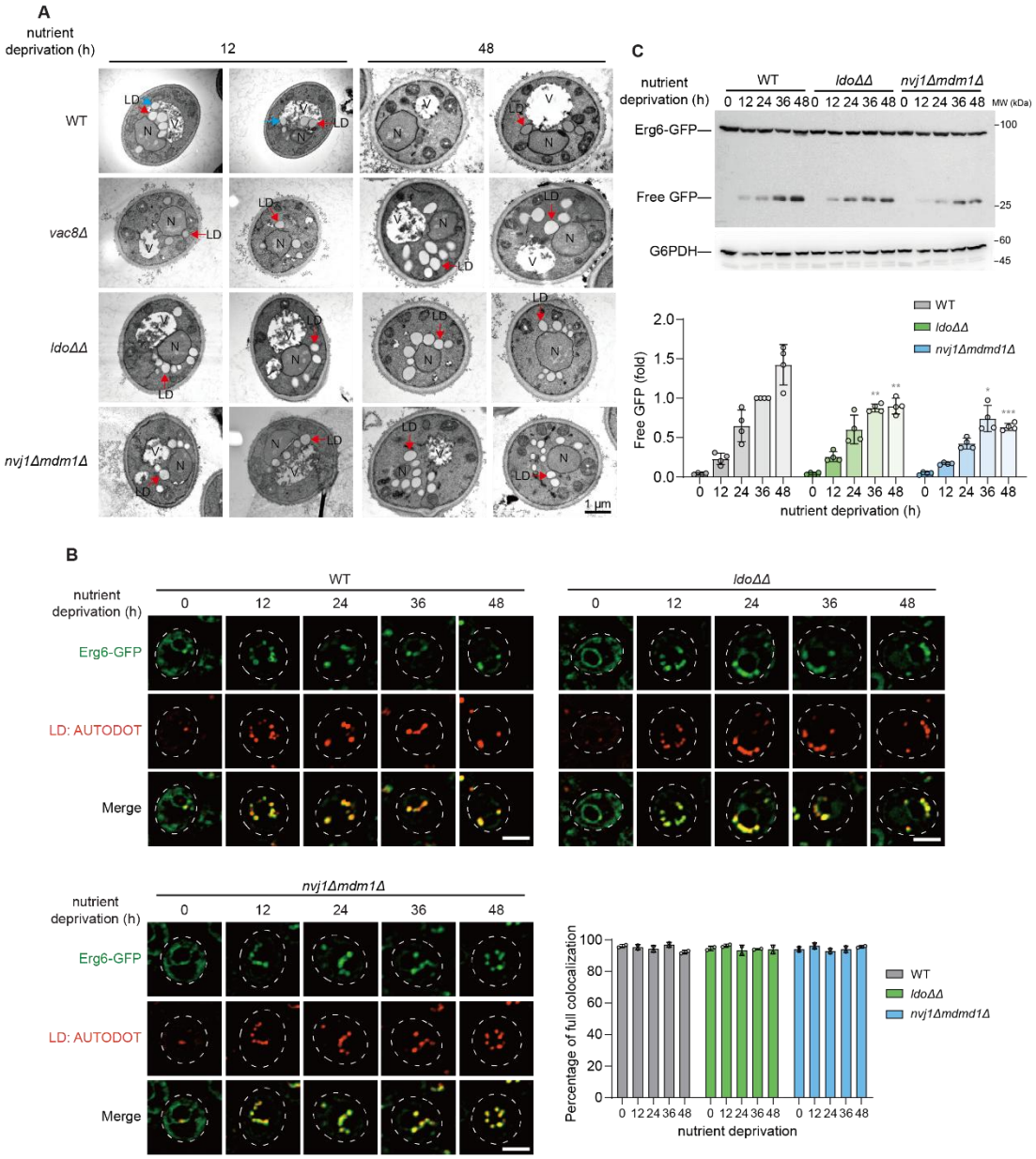
A
nutrient deprivation (h)
12
48
WT
vac8Δ
ldoΔΔ
nvj1Δmdm1Δ
LD
N
V
1 μm
C
nutrient deprivation (h)
WT
ldoΔΔ
nvj1Δmdm1Δ
0 12 24 36 48 0 12 24 36 48 0 12 24 36 48
MW (kDa)
Erg6-GFP—
Free GFP—
G6PDH—
100
25
60
45
Free GFP (fold)
2.0
1.5
1.0
0.5
0.0
nutrient deprivation (h)
B
WT
ldoΔΔ
nvj1Δmdm1Δ
nutrient deprivation (h)
0 12 24 36 48
Erg6-GFP
LD: AUTODOT
Merge
Percentage of full colocalization
100
80
60
40
20
0
nutrient deprivation

Figure S5. Subcellular bearings facilitate efficient LD turnover and adaptation to nutrient stress, related to Figure 7.

(A) TEM images of WT cells collected from 12 and 48 hours of nutrient deprivation. Scale bar, 1 μm. N, nucleus; V, vacuole; LD, lipid droplet; blue arrows indicate lipid droplets undergoing lipophagy.

(B) Left: Live-cell imaging of cells labeled with Erg6-GFP and stained with AUTODOT in WT, *ldoΔΔ* and *nvj1Δmdm1Δ* cells in rich medium and after 12, 24, 36, 48 hours of nutrient deprivation. Scale bar, 2 μm. Right: Quantification of the percentage of full colocalization between LDs and Erg6-GFP in WT, *ldoΔΔ* and *nvj1Δmdm1Δ* cells. Data shown are representative of experiments repeated twice and represented as mean ± SD (n=2 independent experiments).

(C) Western blots of protein extracted from WT, *ldo16Δldo45Δ*, and *nvj1Δmdm1Δ* with Erg6-GFP. The relative amount of free GFP liberated from total Erg6-GFP reflects lipophagy activity. Data are representative of four independent experiments. *, $p<0.05$; **, $p<0.01$, ***, $p<0.001$. Grey asterisks indicate statistical significance for comparisons between WT and respective mutant cells at the same time point.

Figure S6

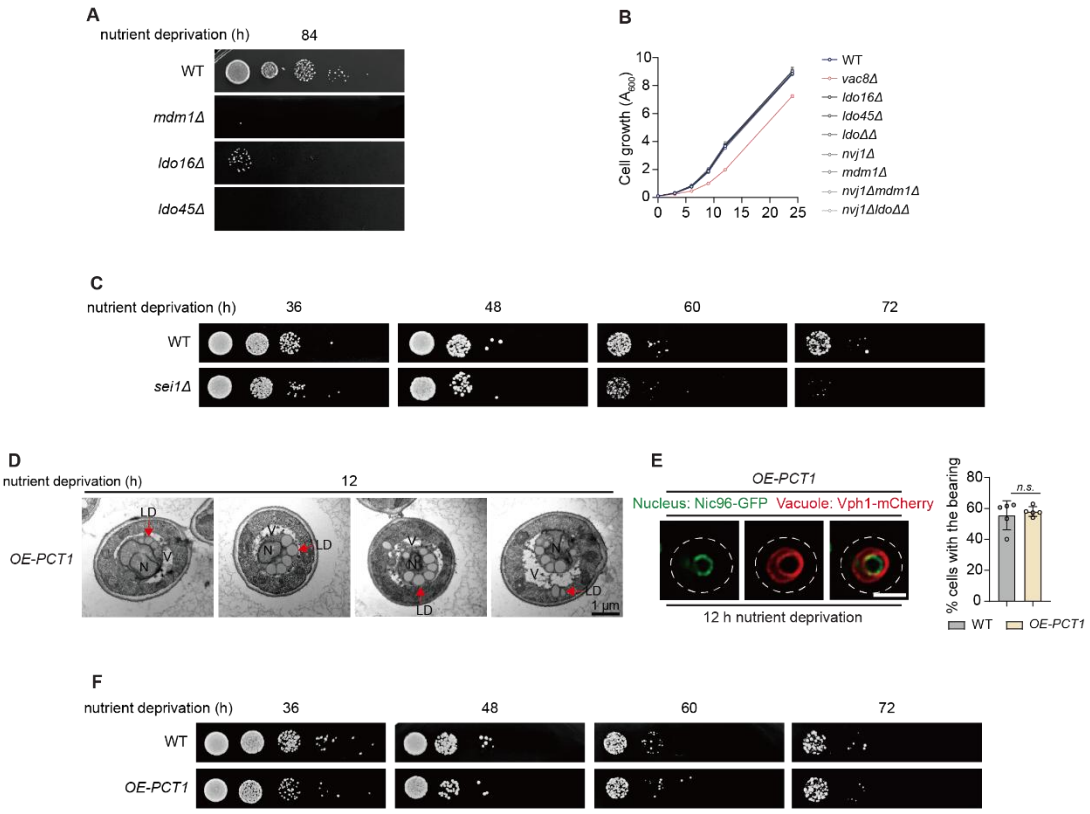
A
nutrient deprivation (h)
84
WT
mdm1Δ
ldo16Δ
ldo45Δ
B
Cell growth (A_{600})
WT
vac8Δ
ldo16Δ
ldo45Δ
ldoΔΔ
nvj1Δ
mdm1Δ
nvj1Δmdm1Δ
nvj1ΔldoΔΔ
C
nutrient deprivation (h)
36
48
60
72
WT
sei1Δ
D
nutrient deprivation (h)
12
OE-PCT1
LD
N
V
1 μm
E
OE-PCT1
Nucleus: Nic96-GFP Vacuole: Vph1-mCherry
12 h nutrient deprivation
% cells with the bearing
n.s.
WT
OE-PCT1
F
nutrient deprivation (h)
36
48
60
72
WT
OE-PCT1

Figure S6. Subcellular bearings play a role in cell survival during prolonged nutrient deprivation, related to Figure 7.

(A) Survival of WT, *mdm1Δ*, *ldo16Δ*, and *ldo45Δ* cells after 84 hours of nutrient deprivation. Cells were spotted onto YPD plates and incubated for 24 hours at 30°C before recording survival.

(B) Growth curves of WT, *vac8Δ*, *ldo16Δ*, *ldo45Δ*, *ldoΔΔ*, *nvj1Δ*, *mdm1Δ*, *nvj1Δmdm1Δ*, and *nvj1ΔldoΔΔ* cells cultured in rich medium YPL. Data are represented as mean ± SD (n=3 biologically independent samples).

(C) Survival of WT and *sei1Δ* cells after 36, 48, 60, and 72 hours of nutrient deprivation. Cells were spotted onto YPD plates and incubated for 24 hours at 30°C before recording survival.

(D) TEM images of cells with *PCT1* overexpression (*OE-PCT1*) collected from 12 hours of nutrient deprivation. Scale bar, 1 μm. N, nucleus; V, vacuole; LD, lipid droplet; blue arrows indicate lipid droplets undergoing lipophagy.

(E) Left: Subcellular bearing formation in cells with *PCT1* overexpression, the Nic96-GFP-nucleus, and the Vph1-mCherry-labeled vacuole under 12 hours of nutrient deprivation. Scale bar, 2 μm. Right: Quantification of subcellular bearing formation in WT and cells with *PCT1* overexpression after 12 hours of nutrient deprivation. Data are represented as mean ± SD (n=5 independent experiments; more than 200 cells were quantified). *n.s.*, no significance.

(F) Survival of WT and *OE-PCT1* cells after 36, 48, 60, and 72 hours of nutrient deprivation. Cells were spotted onto YPD plates and incubated for 24 hours at 30°C before recording survival.